SEARCH FOR TETRAHEDRAL BANDS IN YB ISOTOPES

Shumani Maurice Maliage

Thesis presented in fulfillment of the requirements for the degree of Master of Sciences at the University of Western Cape.

Supervisor: Dr. R.A Bark

Dept. of Physics

iThemba LABS

Co-supervisor: Prof. R Lindsay

Dept. of Physics

University of Western Cape

February 2007

DECLARATION

I, the undersigned, hereby declare that the work contained in this thesis is my own original work and that I have not previously in its entirety or in part submitted it at any university for a degree.

Signature: .....

Date: .....

ACKNOWLEDGEMENTS

- I would like to give special thanks to my supervisor Dr R.A. Bark and my co-supervisor Prof R. Lindsay for their support through mentally and financially;
- Dr R.A Bark who has shown immense patience and support as he guided me on the project in the collection of data and subsequent analysis of the data;
- Also I want to thank all the staff of the Department of Physics for giving courage through some difficulty time;
- Honourable people in IT department, especially Sean Murray and Coswell who had helped me to fix sorting program while sorting the data, they deserve more credit because without these people we cannot do anything;
- Finally, I wish to thank all my family members for their unfailing support and encouragement that they devotedly availed to me during the time of my studies;
- Ndi do vha nda livhuwa vhone vha matongoni, kha zwothe zwe vha tikedza uri ndi zwi bveledze u I tela vhadaho uri vha sa tambule, Ndaa vhavenda.

SEARCH FOR TETRAHEDRAL BANDS IN YB

Shumani Maurice Maliage

KEYWORDS

Beta bands

Dipole

Gamma bands

Negative parity bands

Tetrahedral bands

Positive parity bands

Quadrupole

Rotational bands

Vibrational bands

Ytterbium

SEARCH FOR TETRAHEDRAL BANDS IN YB ISOTOPES

Shumani Maurice Maliage

iThemba Laboratory for Accelerator Based Science, P O BOX 722, Somerset West 7129 South Africa

Abstract

Calculations by Dudek et al. predict shell gaps for tetrahedrally shaped nuclei at various proton and neutron numbers. ^{160}Yb is expected to be a favourable nucleus, with tetrahedral bands predicted to lie 1 MeV above the ground state. A search for such states has been performed using the Afrodite Ge detector array at iThemba LABS. A 73MeV ^{16}O beam bombarded a ^{147}Sm target of thickness 3mg/cm^2 to produce ^{160}Yb at low spin and high excitation energy. After analysis of the data, new rotational bands have been added to the level scheme. Although these bands are in the expected energy interval for the tetrahedral states, they do not show the expected decay properties of the tetrahedral bands. Rather, we interpret them as vibrational γ and β bands.

Contents

List of Figures

List of Tables

CHAPTER 1

Introduction

Due to the combination of a short-range nuclear force, a long-range repulsive Coulomb force, and centrifugal forces, the nucleus can take a variety of different shapes. Such shapes can possibly be spherical, oblate or prolate quadrupole deformations, octupole and tetrahedral shape. The most common shapes are the quadrupole shapes. A positive intrinsic quadrupole moment means that the nuclear shape is prolate, with its polar radius longer than its equatorial radius. On the other hand, a negative quadrupole deformation is one in which the nucleus has an oblate shape, with the equatorial radius longer than its polar radius, as shown in Fig 1.1,

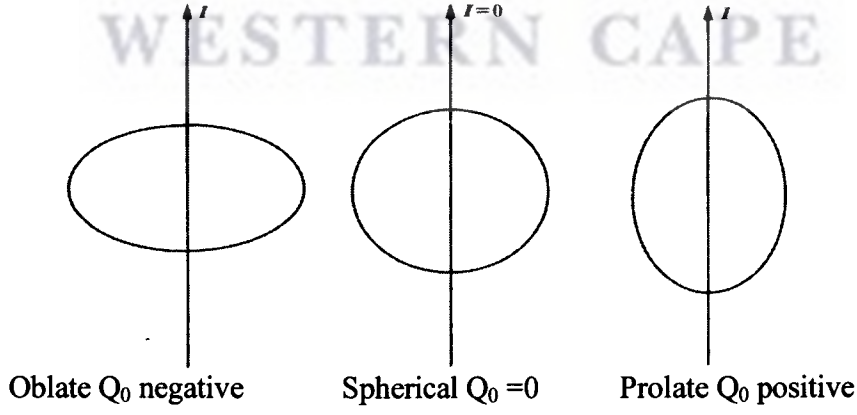

Figure 1.1*: Intrinsic quadrupole moments Q_0 [Bur79]*

The tetrahedral shape is rare in atomic nuclei and can be described as a pyramid like structure with rounded edges and corners and four equilateral three-sided surfaces as depicted in Fig 1.2.

The main goal of this project was to search for tetrahedral shape in the ^{160}Yb isotope by investigating the rotational bands in this nucleus.

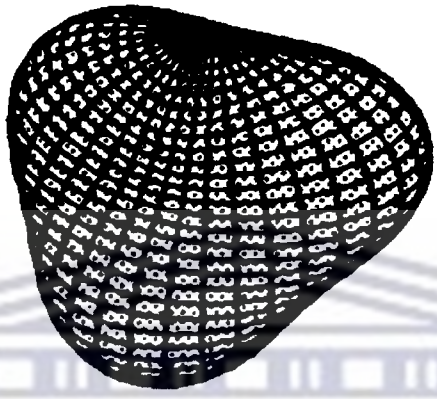

Figure 1.2: *Diagram representing a tetrahedral shape [Dud02]*

1.1 Nuclear surface deformation

In general, the shape of nuclei may be described in terms of an expansion of spherical harmonics, weighted by the coefficients $\alpha_{\lambda\mu}$

$$R(\theta,\phi) = R_0\left\{1+\sum_{\lambda\mu}\alpha_{\lambda\mu}Y_{\lambda\mu}(\theta,\phi)\right\} \qquad 1.1$$

where $R(\theta,\phi)$ is the distance from the centre of the nucleus to the surface at angle (θ,ϕ),

R_0 is the radius of the spherical sphere and $Y_{\lambda\mu}(\theta,\phi)$ are the spherical harmonics. The

coefficients α_{00} describe the monopole shape corresponding to a sphere, since Y_{00} is a constant. The coefficient $\alpha_{2\mu}$ describes the quadrupole shapes of the nucleus, while $\alpha_{3\mu}$ describe the octupole shapes, of which is α_{32} a special case, corresponding to the tetrahedral shapes.

Dudek et al. [Dud02] predicted where the tetrahedral bands might be found. Fig 1.3 shows proton single particle energies calculated by Dudek et al. [Dud03] as a function of the tetrahedral deformation parameter α_{32}. A large gap is seen at particle number 82, corresponding to vanishing tetrahedral deformation. Such shell gaps give rise to stable deformations because there are no nuclear forces acting on the deformation of the nucleus. At particle numbers 70 and 90, gaps are also seen corresponding to a tetrahedral deformation with α_{32}=0.26. The calculated shell gaps are similar for protons and neutrons and are appropriate for heavier mass nuclei. The gaps at Z=70 and N=90 correspond to the nucleus ^{160}Yb, and it is therefore expected to be a favourable case for tetrahedral shapes

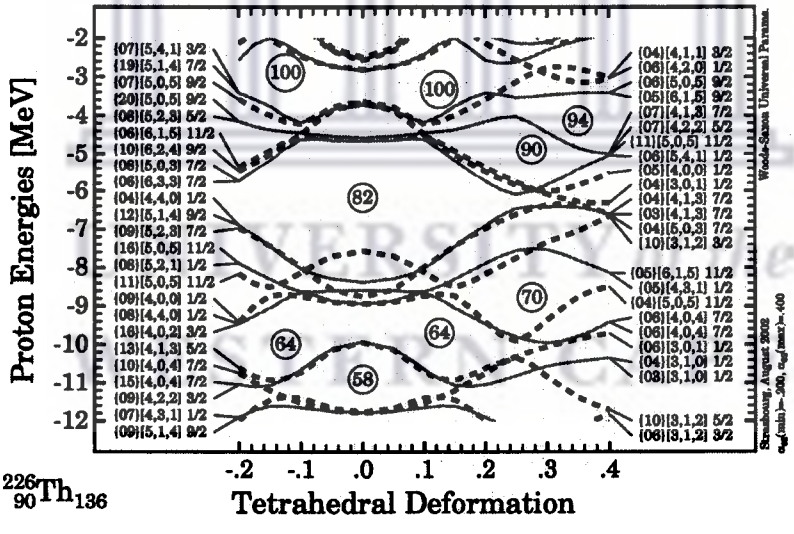

Figure 1.3: *Tetrahedral shell gaps for protons in heavy nuclei [Dud03].*

Ytterbium-160 was calculated by Dudek et al. to have an oblate minimum at β_2=0.22

which lies 100 keV above the prolate ground state, while the tetrahedral minimum was predicted to be approximately 1 MeV higher in energy, as shown in Fig 1.4. Although this is still high in excitation energy, ^{160}Yb is still predicted to be one of the best cases to observe tetrahedral states, which is why it was chosen for the present study.

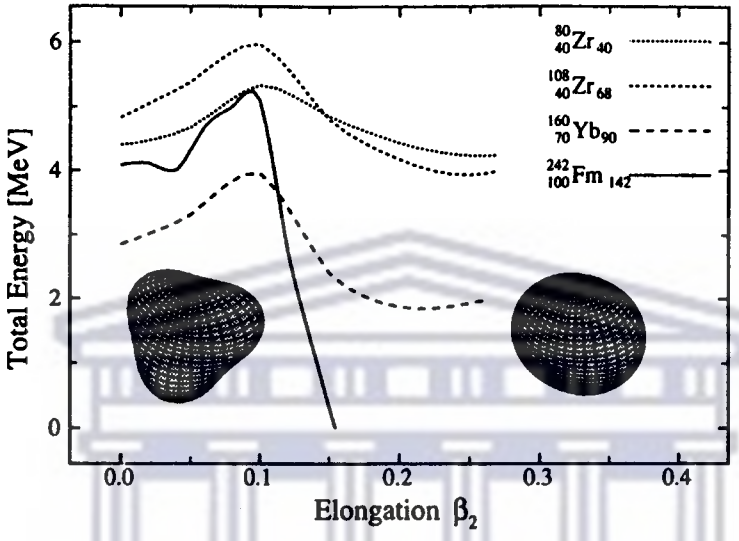

Figure 1.4: *The result of multidimensional minimization of the total nuclear energies projected on the quadrupole deformation axis. Left hand side show an exaggerated tetrahedral shape and the right hand side an oblate shape with β_2=0.2 and γ=60° which correspond to the predicted nuclear deformations of ^{160}Yb [Dud02].*

1.2 Nuclear Rotations

If a nucleus is deformed, quantum mechanically, rotation is allowed not at symmetry axis. There are different types of rotational "bands" depending on the intrinsic nuclear configuration and the nuclear deformation. The ground state bands of even-even nuclei with a quadrupole deformation consist of stretched E2 transitions connecting levels above the 0^+ground state. All the nucleons are paired and the nucleus rotates as a whole. The energies of the levels for a rigidly rotating nucleus are given by

$$E(I) = \frac{1}{2}\Im\omega^2 = \frac{(\Im\omega)^2}{2\Im} = \frac{I(I+1)\hbar^2}{2\Im} \qquad 1.2$$

where $\mathfrak{I}$ represents the effective moment of inertia, ω the angular frequency of the rotation from the rotational energy formula and I the angular momentum. This equation was obtained from the classical rotational energy relation, by substituting the angular momentum with its expectation value: $L^2 = I(I+1)\hbar^2$.

1.2.1 Octupole bands

If a nucleus has a static pear shaped octupole shape $\alpha_{30} \neq 0$, we expect an alternating parity band with levels connected by E1 and E2 transition as shown in Fig 1.5

1.2.2 Tetrahedral bands

In Fig 1.5, the rotation of a tetrahedral nucleus ($\alpha_{32} \neq 0$) is compared with that of a pear-shape $\alpha_{30} \neq 0$. In pear-shaped nuclei a dipole moment is present unlike in the tetrahedrally shaped nuclei. Two parity doublet sequences, with levels connected by stretched E2 transitions are predicted in the tetrahedral nuclei, but now no E1`s are expected. We shall see that this presents a unique signature of tetrahedral shape.

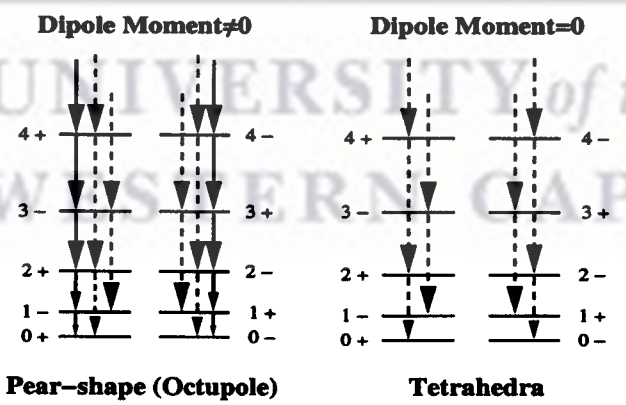

Figure 1.5: *Schematic illustration of expected transitions in rotation bands based on pear-shaped and tetrahedrally shaped nuclei. Dashed lines: quadrupole, solid lines: dipole transitions [Dud02].*

1.2.3 Location of tetrahedral bands

Fig 1.6 illustrates the expected location of hypothetical tetrahedral shape isomers and rotational bands in energy and spin.

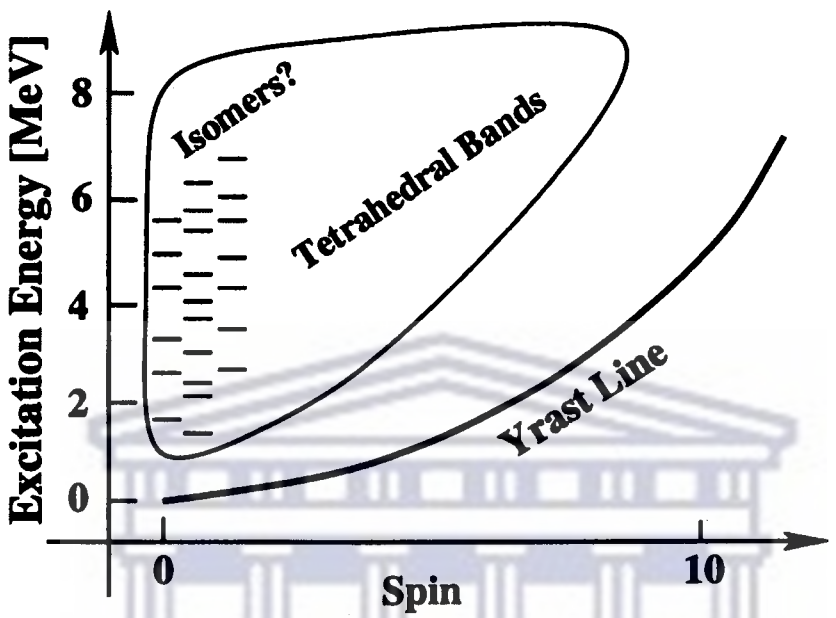

Figure 1.6: *Schematic illustration showing location of hypothetical tetrahedral shape isomers and bands [Dud03].*

This diagram indicates that the tetrahedral bands can lie above to the 1≤E≤g MeV approximately 1 MeV above the ground state, and remain well above the yrast line. (The yrast line constitutes the set of states having lowest energy for a given spin)

1.3 Vibrational Bands

In a similar region of spin and energy expected for the tetrahedral bands, we also expect vibrational bands. The most important nuclear vibrations are quadrupole and octupole vibrations. Quadrupole vibrations in prolate nuclei are categorized into two different vibrations, beta (β) and gamma (γ) vibrations. For β vibrations, the size of the nucleus along the x and y axes of the body fixed coordinate system are always equal to each

other, and the size along the z axis is changing with respect to time. Such vibrations have no angular momentum, they have states with K = 0 and spin and parity of 0^+, 2^+, 4^+ etc. For gamma vibrations, the vibrations change in x and y axes. Such vibrations carry two units of angular momentum. The states have K = 2 with spin and parity of 2^+, 3^+, and 4^+.....

The lowest vibrational band structure for a prolate quadrupole deformed even-even nucleus is shown in Fig 1.7, which are labelled by the set of quantum number K, n_2, n_0. (n_2 and n_0 are the oscillation number of the vibrations, given by $n_\lambda = \sum_\mu n_\mu = 0;1;2$, where λ is the integral and n_μ is the number of oscillation quanta in a state (λ, μ) and K define the spin projection of the vibrational state).

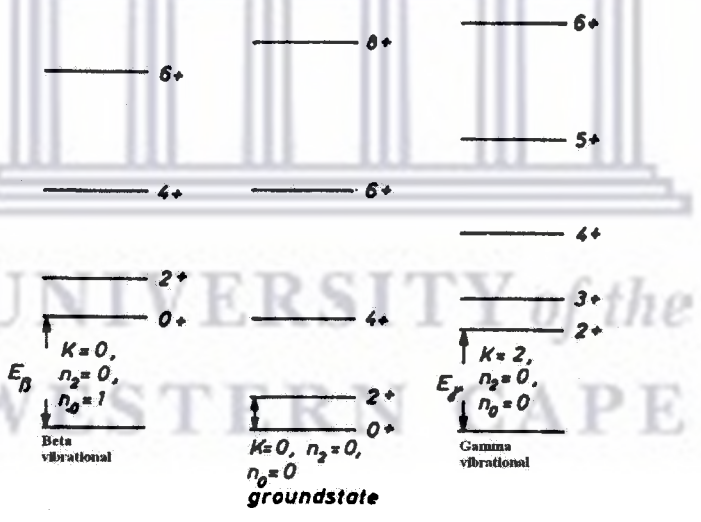

Figure 1.7: *The typical band structure for a deformed even-even nucleus. Phonon n_β and n_γ directed to the types of vibration*

An octupole vibration ($\lambda = 3$) carries three units of angular momentum and has negative parity. Fig 1.8 shows an example of an octupole vibrational band in ^{236}U [Zay87].

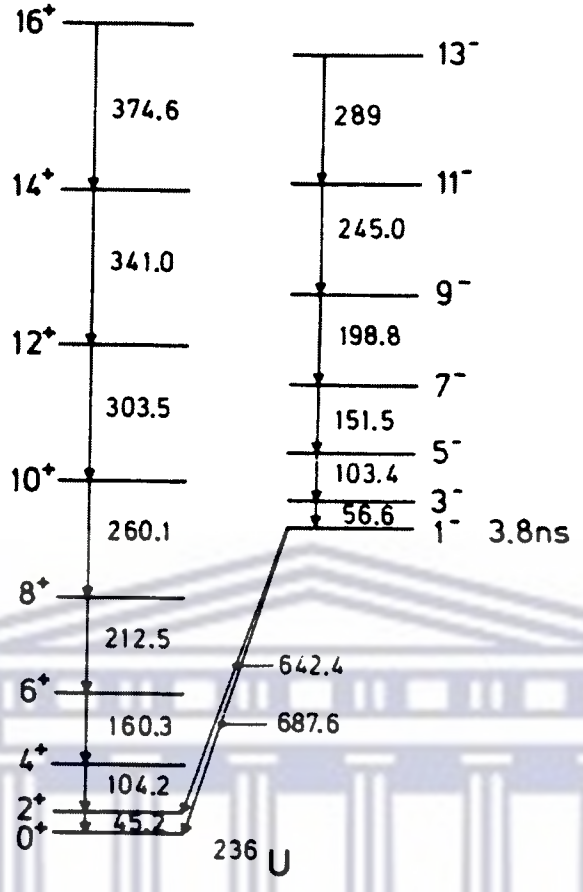

Figure 1.8: *Level scheme of isotope ^{236}U [Zay87].*

Thus we see that none of the competing vibrational bands have a decay pattern that resembles that of the tetrahedral band, and the signature of a tetrahedral band should be rather unique. The challenge is to populate a band that is predicted to lie at excitation energy high above the yrast line.

CHAPTER 2

Experiment and Experimental Equipment

2.1 Creation of ^{160}Yb

A heavy-ion fusion evaporation (FE) reaction was used to create the radioactive nucleus ^{160}Yb. In this reaction, fusion occurs when the incident particle or projectile has enough energy to overcome the Coulomb barrier that exists between it and the target nucleus. The heavy ion fusion evaporation process is explained below.

(a) The beam is accelerated in energy of 73MeV, which is enough to overcome the Coulomb barrier.

(b) The projectile and the target nucleus fuse together in a very short time interval of 10^{-20}s [Won90]. After fusing, a loss of identity of the two original nuclei occurs, because of the numerous interactions of many nucleons between the incident particle and the target nucleus. The two nuclei form a single nucleus, called a compound nucleus, with high excitation energy, which subsequently decays by emitting neutrons (n), protons (p) or alpha particles (α). The emitted particles carry away most of the excitation energy from the compound nucleus. The decay process is determined by the amount of excitation energy available in the system.

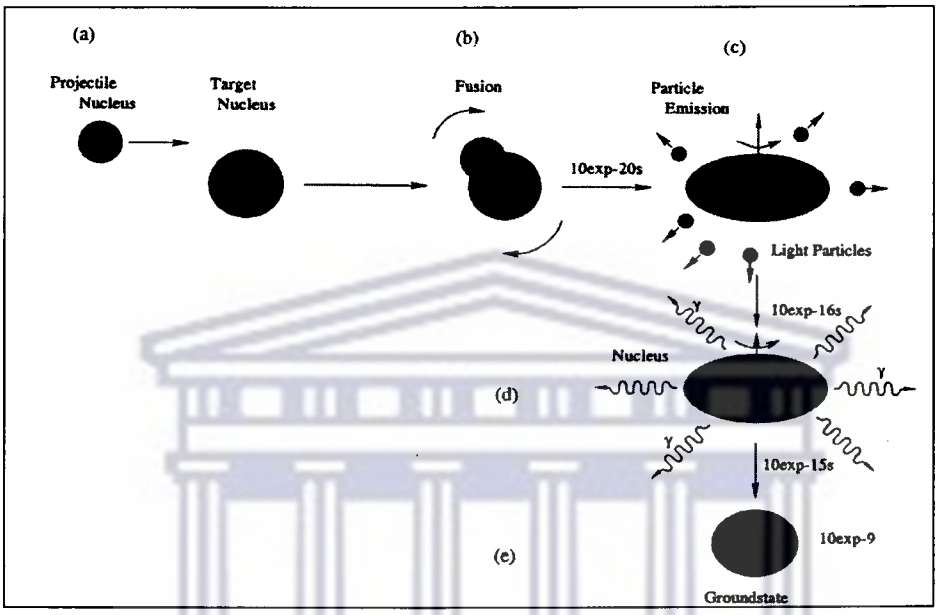

Figure 2.1: *Schematic representation of the formation and decay of a compound nucleus through an FE reaction.*

Finally the nucleus decays to the ground state in a time greater than a few hundred picoseconds by emitting gamma rays. The entire process, shown in Fig 2.1, is also indicated in the excitation energy and spin diagram shown Fig 2.2. In this case the γ-ray decay process is subdivided into two different stages, the so-called statistical emission where a large amount of energy in the form of E1 γ-rays is released and discrete emission which involves the cascades of γ-rays near the yrast line where large amount of angular momentum is removed from the system.

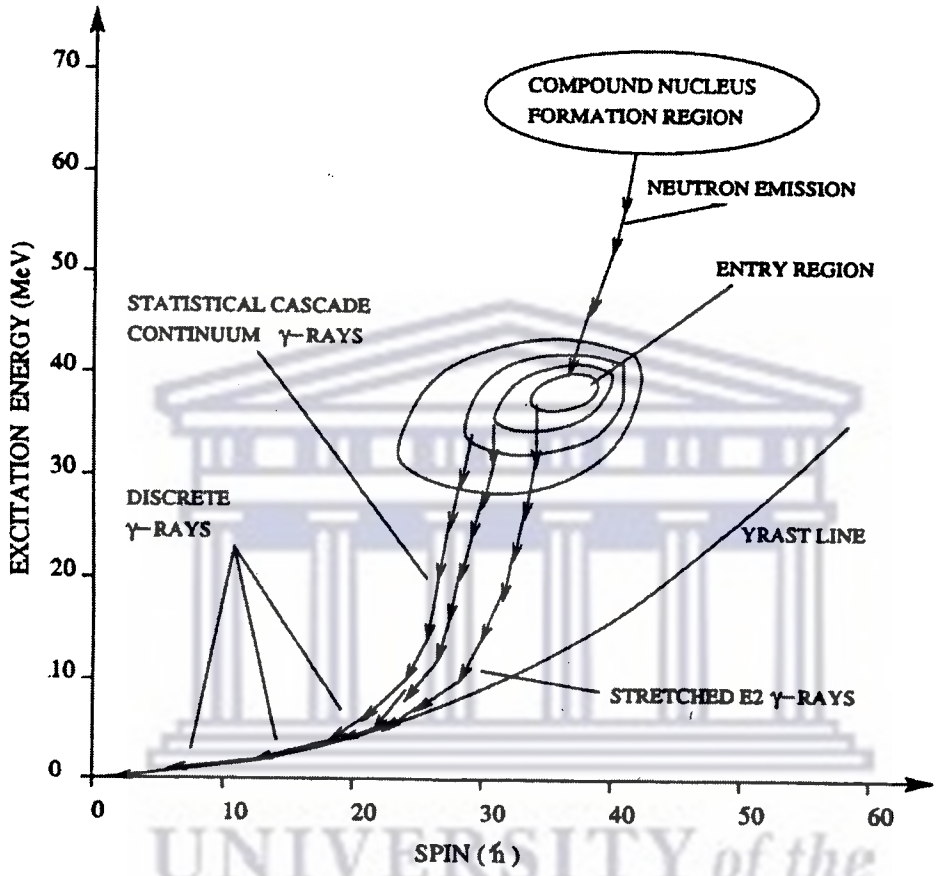

Figure 2.2: *Schematic representation of how an excited compound nucleus formed in FE reaction decay.*

2.2 Observing γ-rays from non-yrast states

We want to enhance the population of non yrast states, as this is where the tetrahedral bands are expected to lie.

The reaction used in this experiment employed a ^{16}O beam of 73MeV energy to bombard a ^{147}Sm target. A thick target of about $3mg/cm^2$ was used in order to stop the reaction

products from recoiling out of the target. The compound nucleus, $^{163}Yb_{93}$, in a highly excited state, may decay initially by evaporating 3 neutrons and forms the residual nucleus ^{160}Yb, which was the nucleus of interest. The nucleus is stopped by the time the nuclear decay reaches spin ~20ħ. Gamma rays emitted from states below this spin will not be Doppler broadened by the motion of the nucleus, thus improving the energy resolution for the states of interest, which were expected to lie at low spin. The excitation function for the reaction is given in Fig 2.3, as calculated using the statistical model code PACE2 [Gav93]. The predictions were used to select the beam energy appropriate to perform the experiment using this reaction.

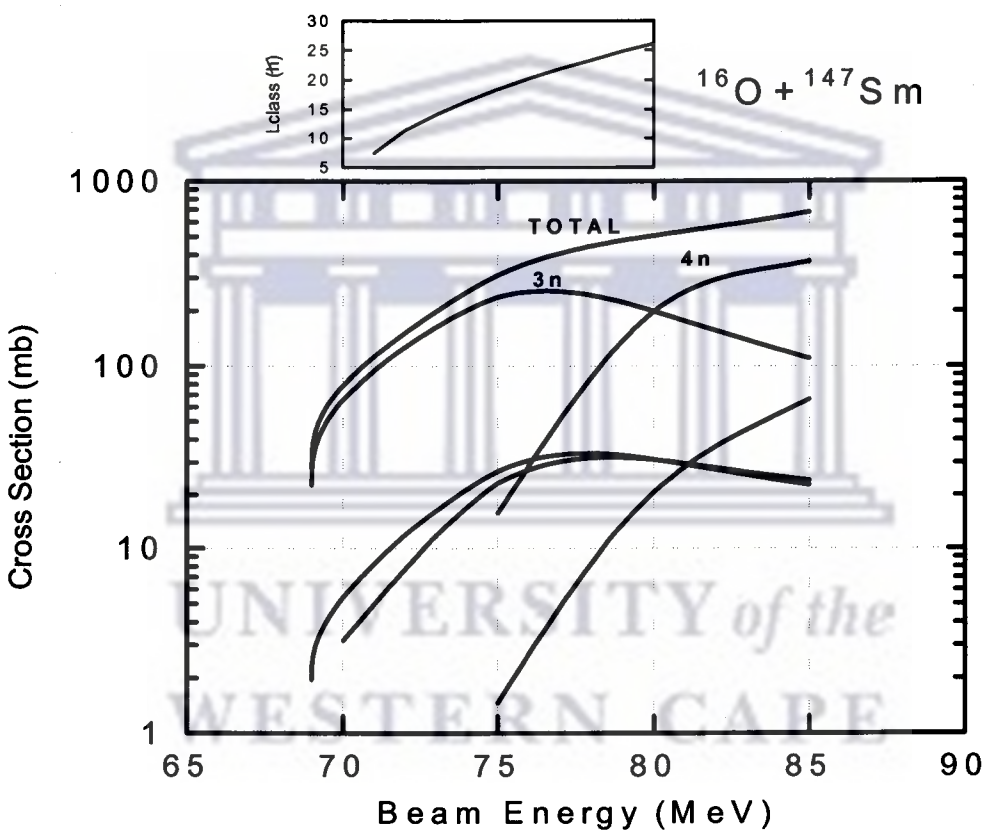

Figure 2.3: *The calculated cross section and for the reaction that has been used in this experiment performed with the AFRODITE array at iThemba LABS. The small diagram above indicates an approximation of the angular momentum of the compound nucleus as a function of the beam energy in the relevant beam energy interval.*

At 73 MeV energy, the beam would lose sufficient energy while transiting the target so that all the projectile nuclei that cross the Coulomb barrier contribute to the compound

nucleus formation, but at lower excitation energy, thereby enhancing the population of the low-spin states in ^{160}Yb. The gamma rays emitted from the evaporation residue, ^{160}Yb, were detected with the Ge detectors of the AFRODITE array shown in Fig 2.4. There are two types of high purity germanium (HP Ge) detectors. These are 6 LEPS (low energy photon spectroscopy) detectors, which are optimized to detect low energy γ-rays (below ~200 keV) and X-rays, and the 8 clover detectors, which are suited to detect low and high energy γ-rays. AFRODITE has a target chamber, which is made of an aluminium frame with 19 facets. All these facets on the target chamber have their own specific use. Two square facets at angles 0° and 180° were connected to the beam line, the one facet which was at an angle 90° perpendicular to the beam direction was used to support the hydraulic target positioner or target ladder and the remaining facets were used to allow the particle to pass through in order to interact with all 8 Clover and 6 LEPS detectors situated at different angles, but 6 LEPS were used instead of 8 LEPS which left two facets empty. Every clover detector is housed in a Compton suppression shield, that is made up of bismuth germanate which was used to detect Compton scattered gamma rays that escape from the clover detector. Such events are rejected by the signal processing hardware (see section 2.4).

The target, a ruby and an empty frame used for focussing the beam were loaded on the aluminium target. The target ladder was mounted on a haudraulic positioner, which can be controlled from the control room during the focussing of the beam. The beam was positioned from the control room by focusing it first through a hole in the center of the ruby.

Even if the beam is focussed through the center-hole of the ruby, the beam may still have a halo, which might interact with the aluminium frame of the target. If an empty target frame is placed in the target position and an increase in the count rate of the detectors is observed, the halo is interacting with the target frame. Once this count rate was reduced by additional focussing, the target (^{147}Sm) was positioned at the beam location. The reaction commenced when the beam and target nuclei interact each other. Once reactions occur, the germanium detectors detect the γ-rays and produce signals which are treated by

the processing electronics modules. Then the information is conveyed to the computer system in the data room where the energy and the other spectra are of the detected γ rays observed.

Figure 2.4: *AFRODITE array with its frame, which supports the LEPS and clover detectors [Afr05].*

Fig 2.4 indicates how the clover and LEPS detectors are arranged in the AFRODITE array at iThemba LABS.

2.3 Clover and LEPS detectors

2.3.1 Clover detectors

The clover detectors are made up of four separated coaxial n-type germanium crystals,

which are ~0.2mm apart as depicted in Fig 2.5. These crystals are 70mm in length, 50mm in diameter and 36mm in tapering length. Their front face has approximately square shape with 41mm sides, see Fig 2. 5. Each crystal has its own preamplifier in order to take the information from it separately. If the gamma rays are Compton scattered from one crystal to an adjacent one, the energy detected in both crystals can be added back to get the full energy of the gamma ray. This is known as "add-back". The clover detector Dewars (Fig 2.6) are filled automatically with liquid nitrogen (LN_2).

2.3.2 Compton Suppression

The main use of the BGO Compton suppression shield was to reduce the unwanted γ-ray Compton background. When the gamma ray interacts with the detector material, it can be fully absorbed by the clover detector or Compton scattered out of the clover detector and then may be detected by the BGO. This bismuth germanate (BGO) is a pure inorganic scintillator. The large atomic number of Bi (Z=83) and high density of BGO (7.3 g/cm^2) make it possible for the detection of gamma rays with high efficiency. Gamma-rays detected in the shield are used to veto γ-rays detected simultaneously in the clover detector, thereby suppressing the Compton scattering events.

The BGO Compton suppression shield has the shape of pyramid as depicted in Fig 2. 7. It also has a heavy metal collimator in front of it, which prevents gamma rays from the produced nuclei interacting directly with the BGO material, because once they interact with the BGO material they will veto any gamma rays that have been detected directly by the Ge detector when the reaction occurs.

2.3.3 LEPS detectors

LEPS detectors consist of a single crystal of p-type Ge. Each crystal is electrically segmented into four quadrants. LEPS detectors have a maximum efficiency at low energy below ~200 keV [New98]. Only 6 LEPS detectors were mounted and arranged in the

array at different angles. The LEPS detector Dewars are filled with liquid nitrogen (LN_2) from the storage tank for every 24 hrs.

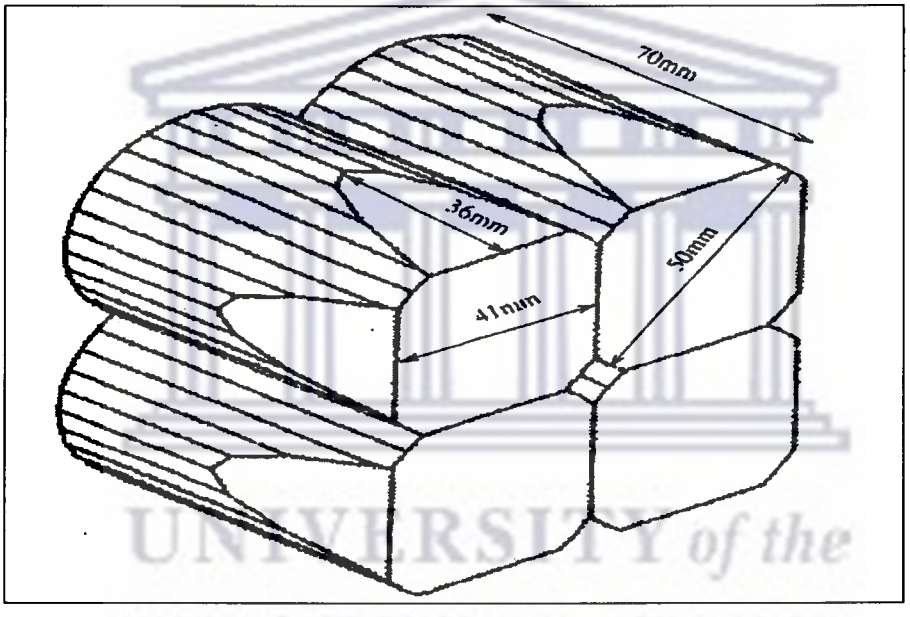

Figure 2.5: *The four-leaf HPGE crystals are crafted and packed together in a clover detector [Jon95].*

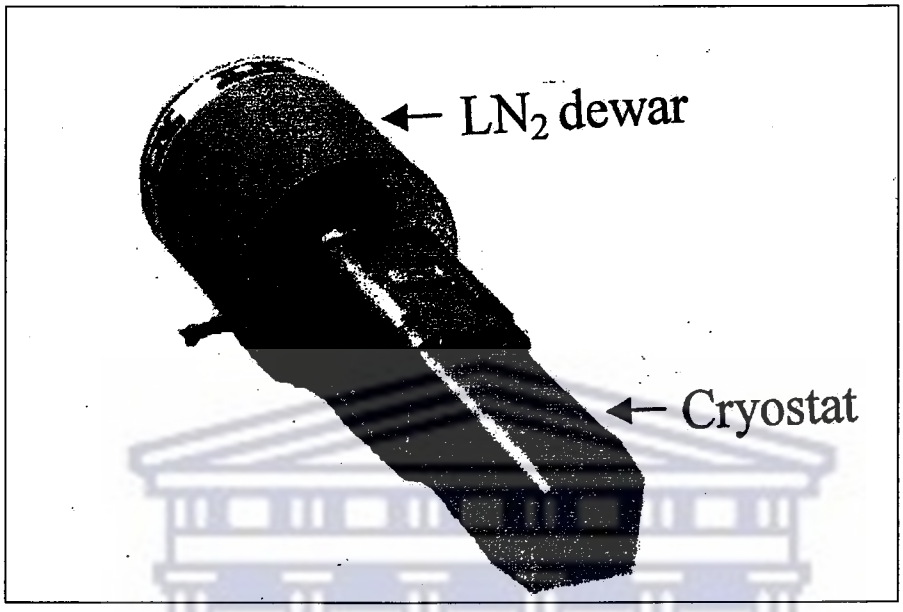

Figure 2.6: *A clover detector, showing the tapered rectangular cryostat and cylindrical nitrogen (LN2) Dewar [Duc99].*

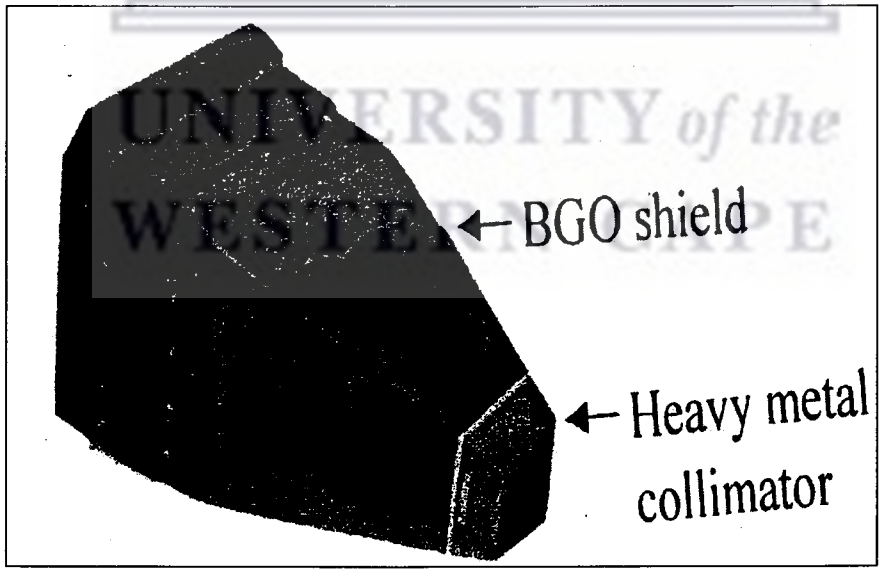

Figure 2.7: *A BGO Compton suppression shield, showing the tapered heavy metal collimator at the front end [Duc99].*

2.4 Electronics and Data acquisition system

The iThemba LABS data acquisition system is based on the MIDAS software package.

2.4.1 Electronics

In this experiment six LEPS and eight clover detectors were used to detect the gamma rays emitted when a reaction occurs. Referring to Fig 2.8, the LEPS detectors provide four channels per detector; the N568 amplifiers amplify the signals from the LEPS preamplifiers and shape them in a convenient form for both linear and fast signals. The fast signal produced by the amplifier then goes to the Constant Fraction Discriminator (CFD) where the signal is changed to a logic form and then goes to the FAN IN circuit which accepts input signals from all the 4 channels to form an "OR" output. After passing through a gate and delay generator (G & DG), the "OR"ed LEPS signals are fed into the multiplicity unit which gives a logic output depending on the number, (or multiplicity) of not zero inputs. The fast signals also go to the Gate and Delay generator (G & DG) which delays the signals until after the arrival of a start signal for the 4418/T TDC, where the LEP times are measured.

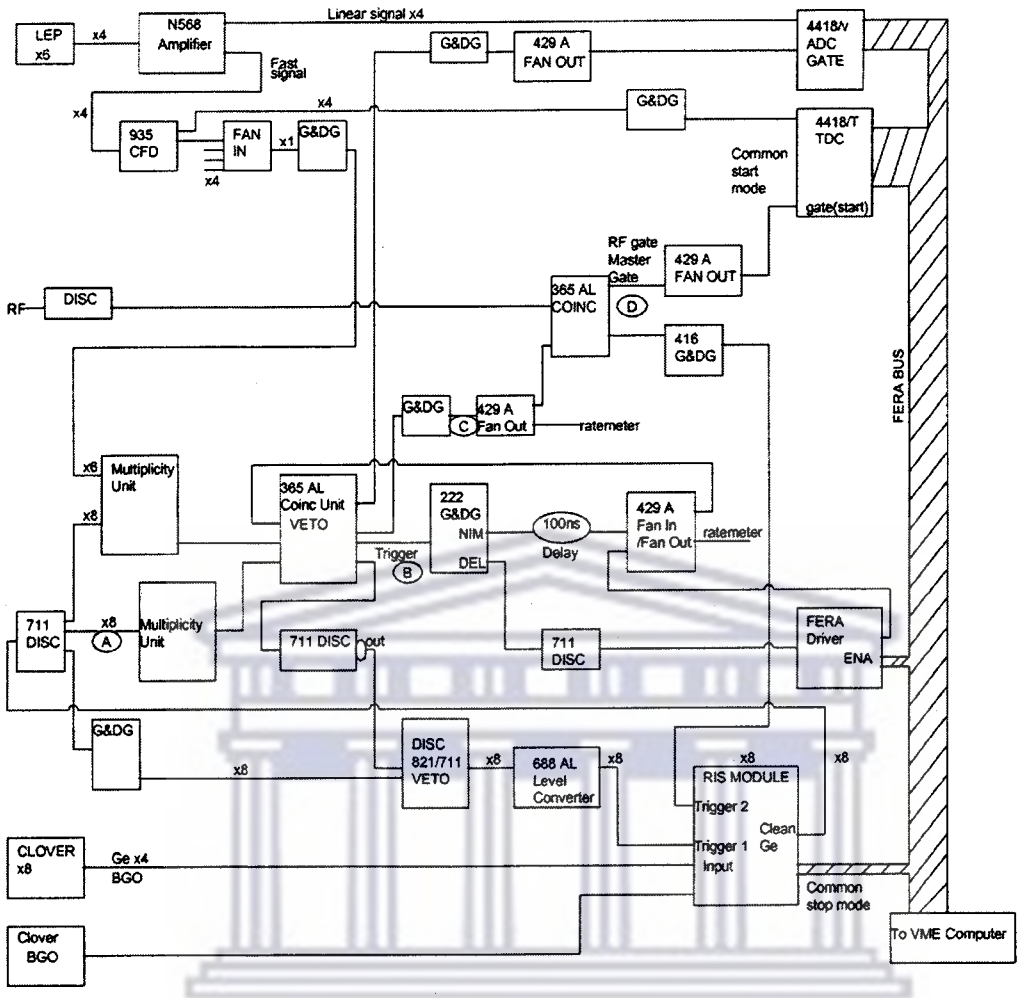

Figure 2.8: *AFRODITE array electronics*

The "RIS" modules handle the signal processing for the clover detectors. These modules have integrated circuits, which perform many of the functions already described for the LEPS, in one unit. It includes the standard fast-slow processing and the anti-Compton veto of events with a BGO signal as shown schematically in Fig 2. 9 and 2.10, to produce the "Clean Ge" signal. The "Clean Ge" signal is fed to two multiplicity units, the first of which was set to 2, i.e. the trigger demanded that two suppressed clovers had fired in coincidence. The second unit accepted also logic signals from the LEPS detectors. The output from both multiplicity units may then be "AND"ed in the 365 AL coincidence unit. In this way, more complex trigger conditions could be demanded. For instance if the clover/LEPS multiplicity unit was set to 3, and the clover multiplicity unit set to 2, the

AND of the outputs of the two coincidence units would at least demand 3 detectors, and at least two of which were clovers, to fire in coincidence. Once the trigger was generated, it was fanned out to the various ADC and TDC and RIS modules. One branch gated the Silena 4418/V ADC's, which digitised the LEP's energies. Another branch would enable digitisation of energy and time in the RIS module by gating the clean Ge signal of the RIS module where the signal conversion starts.

Finally, a branch of the trigger fan-out was used to create an RF-gated trigger, which is used both to gate the various TDC's and as the time reference. The timing diagram is shown in Fig 2.11. The cyclotron RF signal provides the time reference. In this experiment, the pulse separation was 366ns. The arrival of two clean Ge signals, Ge1 and Ge2 at the coincidence unit, generates a trigger signal, with fixed length. The width of the clean Ge signals is set to half the time between beam pulses, in this case about 180ns. This defines the coincidence window. In this example, Ge2 is delayed with respect to Ge1, and a delayed trigger is generated, at trigger B (see also Fig 2. 8). The trigger is stretched by a gate & delay generator at C and gated with the RF signal to produce the RF-gated trigger, at D. (see also Fig 2. 8)

Therefore the RF gated trigger signal is fanned out to the LEPS TDC (4418/T) where it serves as a "common start" that starts the time measurement in the TDC. The individual timing signals are delayed so as to arrive after the common start, and each signal "stops" the TDC allowing the time to be measured. The RIS modules also have an internal TDC, but it operates in common stop mode. The RF gated trigger is used as the common stop, by applying it to the trigger 2 input. The RIS modules, 4418TDC `s and 4418ADC `s are readout on a FERA BUS by a VME module called the F2VB and thereafter the data is sent out to a Linux workstation, which writes the data to tape.

During readout, acquisition is inhibited by vetoing the 365AL coincidence unit where the trigger is generated. The diagram in Fig 2.9 and Fig 2.10 are the process occurs in RIS module.

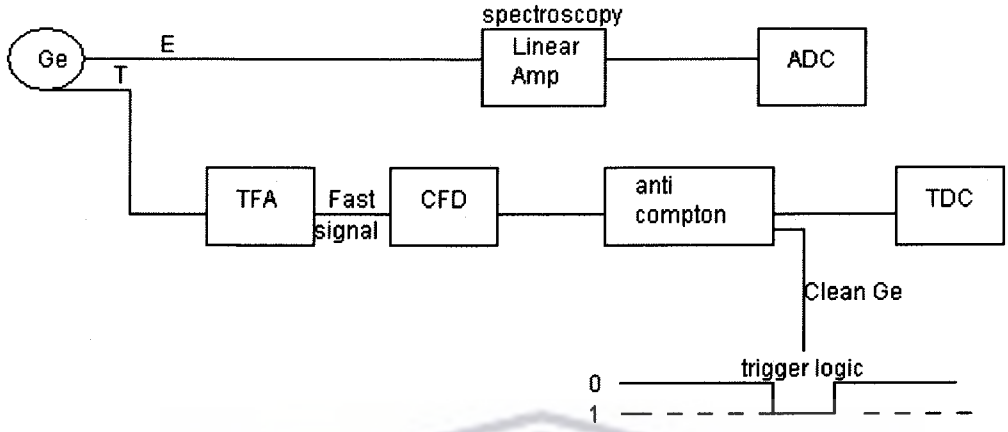

Figure 2.9: *Part of the electronics process occurring in the RIS modules.*

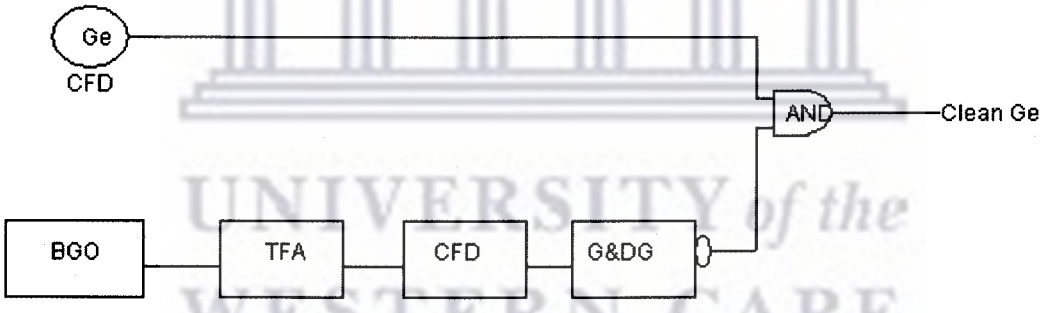

Figure 2.10: *Schematic of the anti-Compton part of the electronics process occurring in the RIS modules with BGO.*

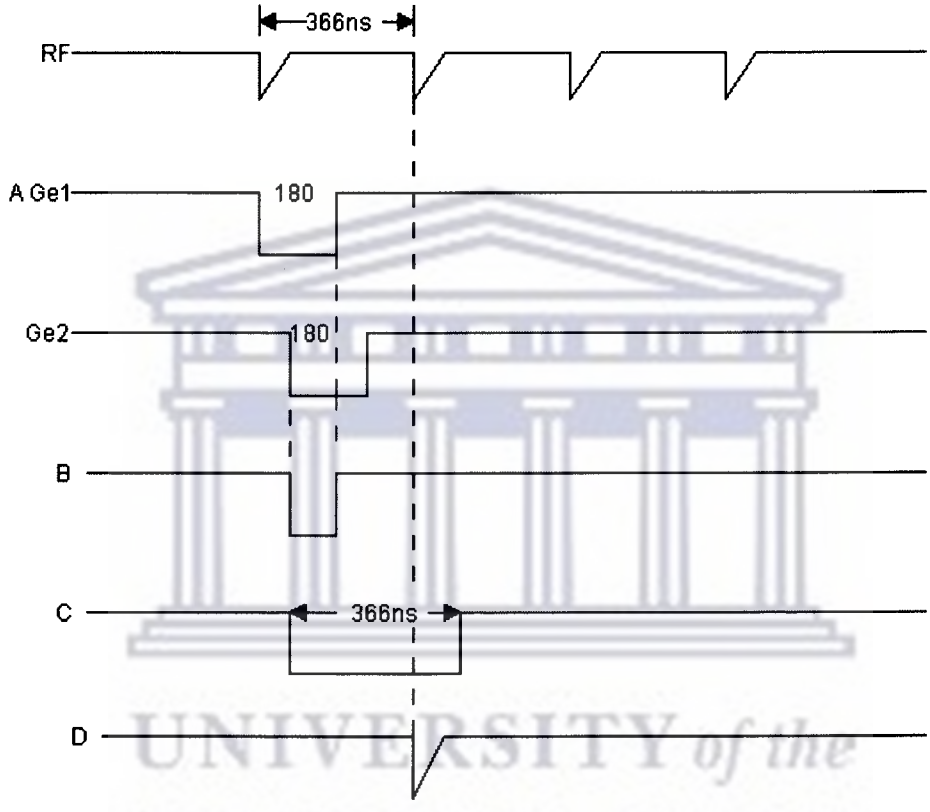

Figure 2.11: *The RF signal coincident with two germanium detector time signals.*

CHAPTER 3

Data Analysis

3.1 Experiment

Two weekends of beam time were allocated for the experiment. The beam used was delivered by the Separated Sector Cyclotron at iThemba LABS. The detectors used in the AFRODITE array were HPGe 8 clovers and 6 LEPS. About 2.9×10^{9} γ-γ coincidence events were successfully collected (onto the magnetic DLT tapes).

3.2 The Energy Calibrations

The energy calibration was done on the first weekend before starting to run the experiment and also after the second weekend, after finishing the experiment, by using ^{152}Eu and ^{133}Ba radioactive sources. When taking measurements, one of the sources was mounted on the target ladder inside the target chamber, and the spectra were recorded. The SFIT program was used to determine the centroids of the photo peaks from the source (^{152}Eu and ^{133}Ba) spectra. The SFIT program automatically finds the centroids of the photo peaks from the source (^{152}Eu) but did not function for the ^{133}Ba source spectra. The program GF3 [Rad95] was used to "manually" fit the centroids of the photo peaks from the ^{133}Ba spectra. In order to determine the energy calibration coefficients and gain matching coefficients, the program SCAL was used to take the peak positions found by

the SFIT and GF3 programs and fit an energy calibration for each detector, of the form $E = a_0 + a_1 x + a_2 x^2$, where x is the channel number.

3.2.1 Energy gain matching

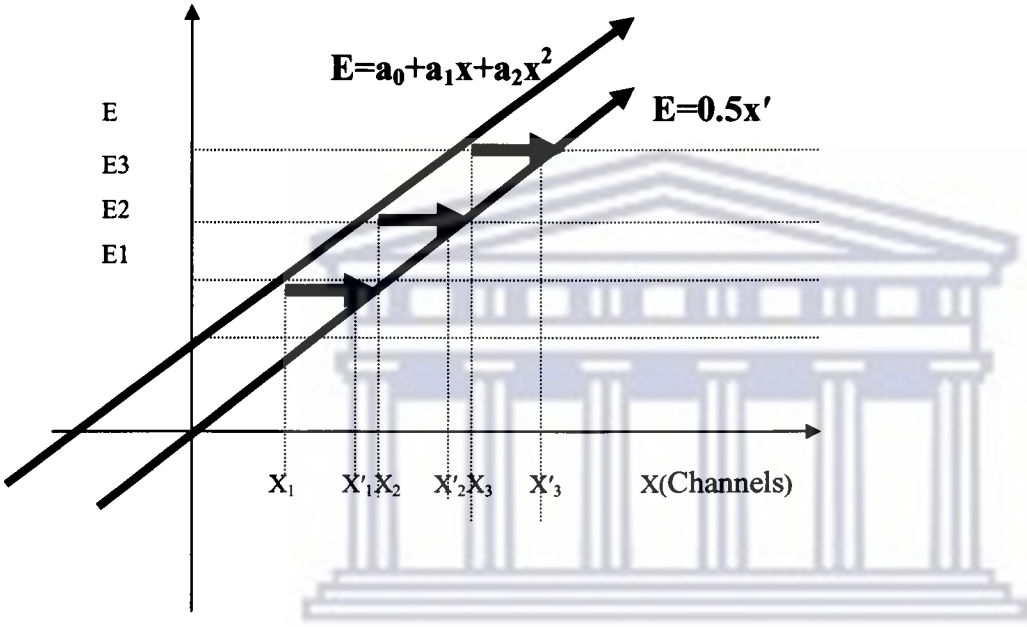

Figure 3.1: *This figure shows how the energy gain match was done. The arrows indicate mapping direction from one equation to the other with X' on the x-axis which shows the new required channels.*

Fig 3.1 shows how the gain matching is performed. For the clover detectors we wanted to map the channels, x, with a quadratic energy calibration of the form $E = a_0 + a_1 x + a_2 x^2$ onto new channels x', with a linear calibration of the kind $E = 0.5x'$. In order to do that we equate the two of energy expressions as follows

$$0.5x' = a_0 + a_1 x + a_2 x^2,$$

which implies that,

$$x' = 2a_0 + 2a_1 x + 2a_2 x^2,$$

This means that every energy calibration coefficient that we obtained must be multiplied by 2 as indicated in the equation above.

The program DOP_COR was used to produce the gain matching coefficients, to map the channels to calibrations of $E = 0.2x$ and $E = 0.5x$ for the LEPS and clovers respectively.

3.2.2 Time gain matching

The time gain matching was done for both LEPS and clover detectors. In order to determine the time gain matching for the clovers, we used the clover time spectra, one of which is depicted in Fig 3.2. It comprises a prompt peak at a channel x_0 and some small peaks extending on the right hand side of it, which represent beam pulses with time separation of 366ns. These pulses have smaller amplitudes than the "prompt" peak since they are caused by γ-rays being detected outside of the coincidence window.

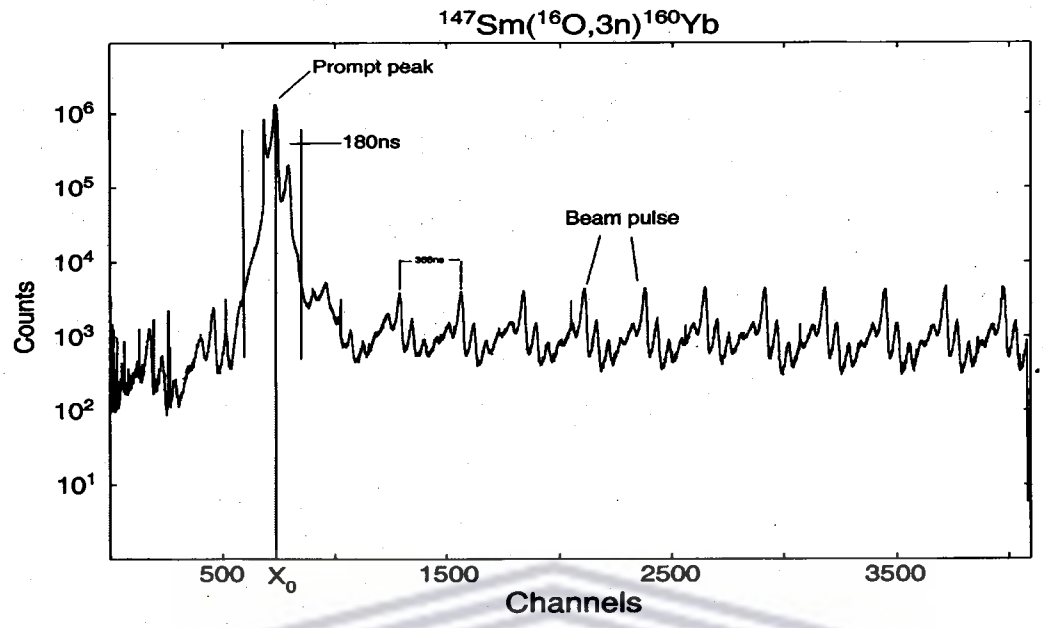

Figure 3.2: *The time spectrum.*

The diagram below shows how the time gain matching was done

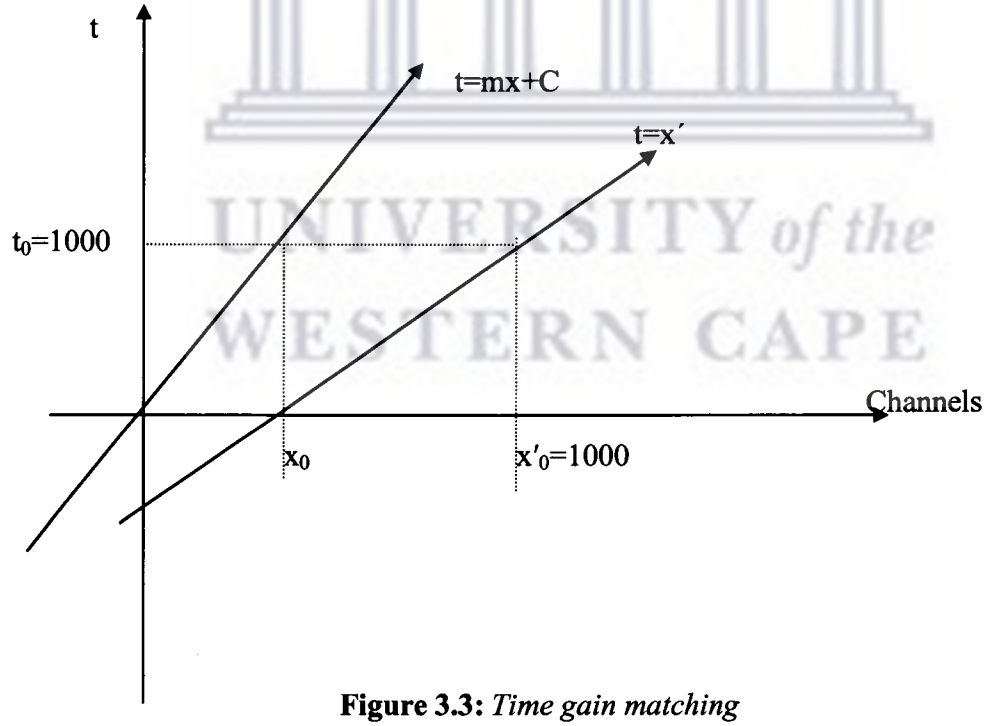

Figure 3.3: *Time gain matching*

First, the time dispersion, m, was determined from the separation of the peaks in the time spectrum. The slope m can be obtained by using: $m = \frac{366ns \times number(pulse)}{(x_i - x_f)}$. where x_i and x_f are the centroids of the initial and final time peaks. The prompt peak at channel x_0 was assumed to occur at time t_0=1000. In this case we want to map the time $t = mx + C$ onto $t = x'$, where x' are the new channels and C is a constant. In order to determine x', we equate the two expressions as follows

$$x' = t = mx + C \quad (1)$$

and especially $$t_0 = 1000 = mx_0 + C, \quad (2)$$

then $$C = 1000 - mx_0 \quad (3)$$

By substituting equation (3) into equation (1), we get

$$x' = mx + 1000 - mx_0 \quad (4)$$

So finally we have $$x' = m(x - x_0) + 1000 \quad (5)$$

In the case of the LEPS, the slope was obtained differently compared with the clovers, because their TDC have fixed dispersion. Some of the LEPS TDC`s had a range of 200ns, the others 1000ns. If the TDC had a 200ns time range, only a single time peak could be observed. Then the corresponding slope for such a TDC was given by

$$m = \frac{200ns}{4096} = 0.0488ns/channel$$

as each LEP TDC had 4096 channels. For the TDC`s which produce 1000ns full scale, $m = \frac{1000ns}{4096} = 0.244ns/channels$.

3.3 Gamma-gamma matrix construction

The calibration parameters that were found were used in the MTsort program which matched the energies and times and then updated a two-dimensional ($E_{\gamma 1}$, $E_{\gamma 2}$) histogram, or matrix. After γ-γ coincidence matrix was created the eg2mat program was used to convert the two-dimensional spectra into a (.mat) Radware format [Rad95], which could be analysed using the GF3 and escl8r program. The γ-γ matrix with dimension of (4096 ×4096) channels and with dispersion of 0.5keV/channels had equivalent to 35000000 of counts for a clover detector as depicted in Fig 3. 4.

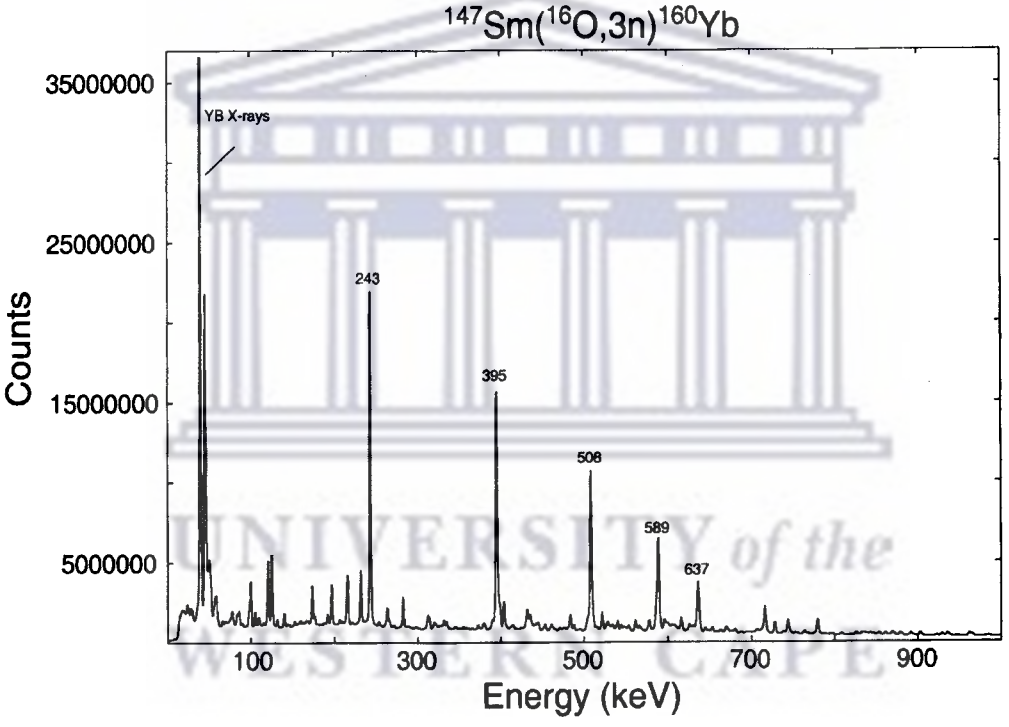

Figure 3.4: *Total projection spectra of clover matrix with background not subtracted.*

3.3.1 Time gates

Fig 3.5 shows a gain matched clover time spectrum. The time increases towards lower values of x, and is represented by an arrow pointing on the left as depicted in the Figure

3.5. Late and early represent the late and early detection of gamma rays by the clover germanium detectors relative to the prompt beam pulse. The time measure occurred in the common stop mode, where the time measurement in the RIS module is started by an individual clean Ge signal (e.g. A in Fig 2.11) and stopped (delayed) by the RF gated master gate (D in Fig 2.11). Thus, the later the signal A occurs, the smaller the time difference with the RF gated master gate, so that "late" signals appear at lower channels than "early" or "prompt" signals.

The bump shown on the left hand side of the prompt peak is caused by x-rays. Because they have relatively low energy, they interact near the surface of the Ge crystal and therefore the charge deposited takes longer to collect, resulting in a delayed signal.

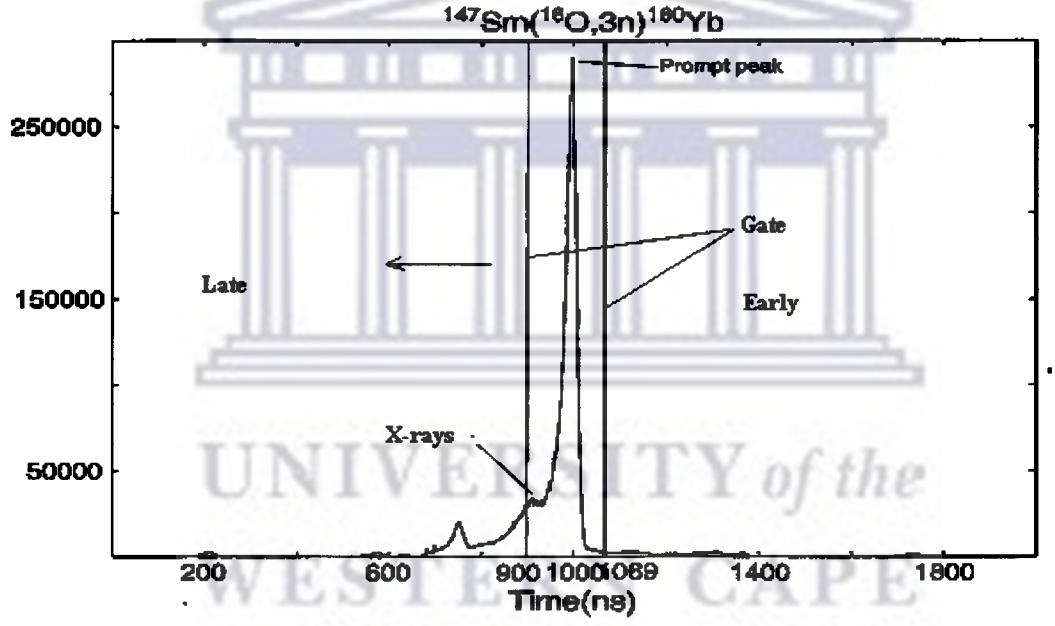

Figure 3.5: *The prompt gate on the gain matched time spectrum*

When the γ-γ matrices were constructed, a gate was set on the clover time, shown in Fig 3.5, to ensure only "prompt" γ-rays contributed to be matrix.

3.3.2 Addback

The clover detector is made up of four crystals, as depicted in the previous section in Fig 2. 6. A γ-ray can be detected in a first crystal, which could then be Compton scattered and detected again by a second crystal. So the energy from the first crystal can be added to the second crystal energy to recover the total energy. This is what we call add back. This add-back is very important because it increases the photo peak efficiency. The program MTsort also carried out the add-back operation.

3.4 Efficiency Calibration

The efficiency Calibration measurements of the LEPS and clover detectors in AFRODITE were performed at the end of the experiment by using ^{152}Eu and ^{133}Ba radioactive sources. These data were recorded in event-by event mode and later sorted offline, in order to perform the add-back of the energies deposited in the various crystal elements. The sources were mounted on the ladder one after another inside the target chamber. The relative efficiency (ε) curve for the 8 clover and 6 LEPS detectors in the AFRODITE array when using ^{152}Eu radioactive source are depicted in the Figures 3.6 and 3.7 respectively. The equation for the efficiency calibration was given as

$$In(eff) = [(A + Bx + Cx^2)^{-G} + (D + Ey + Fy^2)^{-G}]^{-\frac{1}{G}} \quad (6)$$

In equation (6), A, B, and C describe the efficiency at low energies and D, E, and F describe the efficiency at high energies. The relative efficiency curve for both clovers and LEPS detectors was determined using the RadWare Software Effit program [Rad95]. The efficiency for clover and LEPS detectors dropped at energies below 150 keV and 100 keV, respectively. The maximum detection efficiency occurs at 150 keV and 100 keV for clover and LEPS detectors and decreased smoothly as the energy increases.

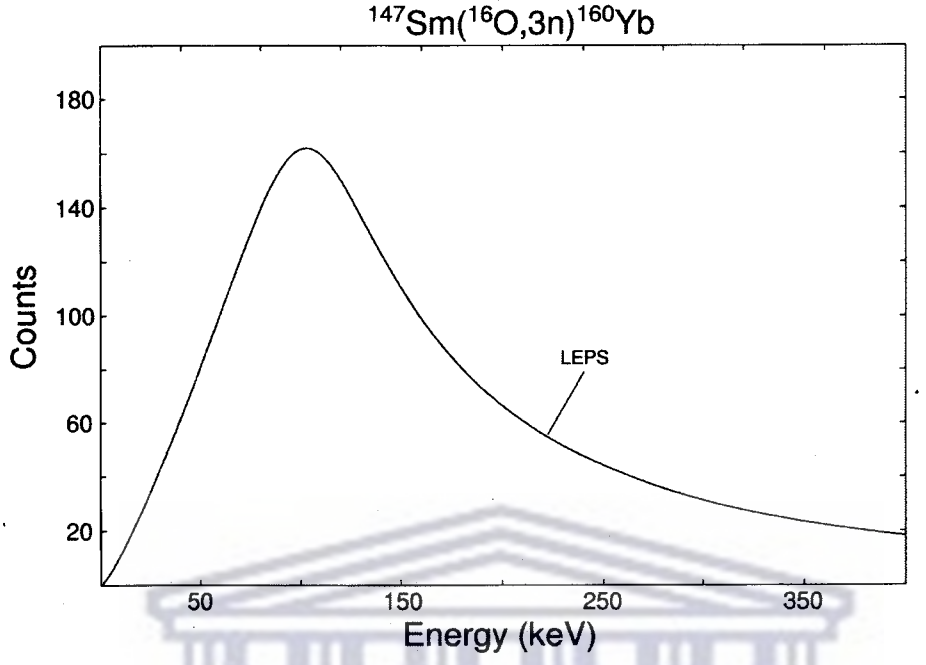

Figure 3.6: *The relative efficiency curve for the 6 LEPS detectors measured with the ^{133}Ba radioactive source mounted on the target ladder in the AFRODITE array.*

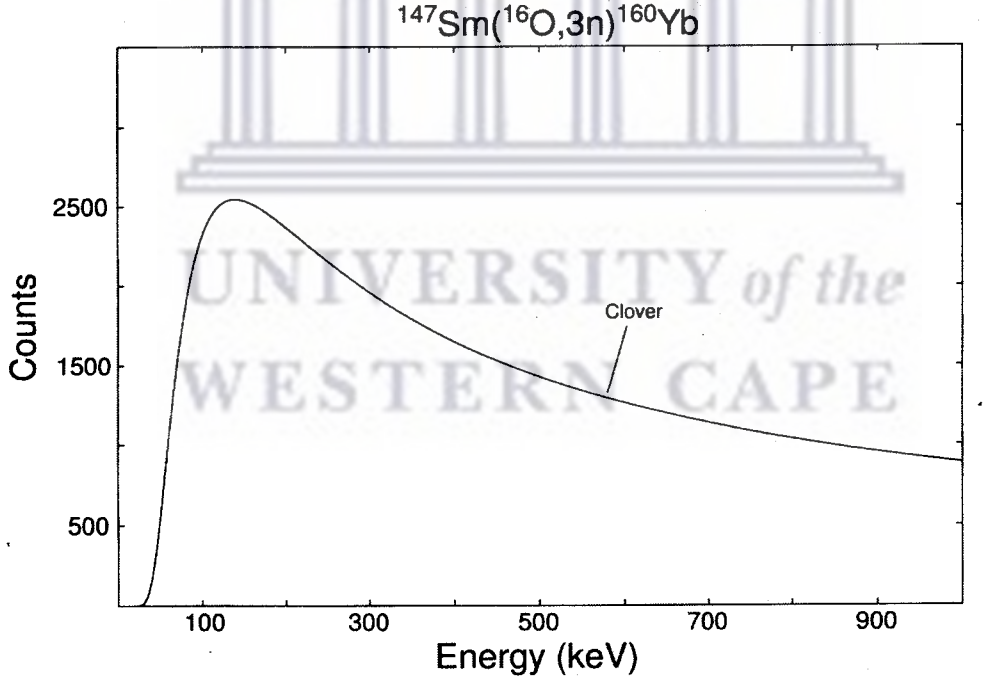

Figure 3.7: *The relative efficiency for the 8 clover detectors measured with the ^{152}Eu radioactive source mounted on the target ladder in the AFRODITE array.*

3.5 Construction of level scheme

The ESCL8r is an interactive program for graphics-based analysis of gamma-gamma data for the deduction of level schemes. It allowed us to display three graphics windows at the same time. Each of those windows has its own specific uses. The first window displays the spectra which were used to build the level scheme, the second window is used to enter the commands in order to tell the program what to do, and the third graphics is used to display the level scheme constructed from the γ-γ coincidence matrix.

3.6 Angular Distribution

Transitions of multipolarity L between the initial and final substates m_2 and m_1 of two levels of spin I_2 and I_1 are depicted in Fig 3. 8.

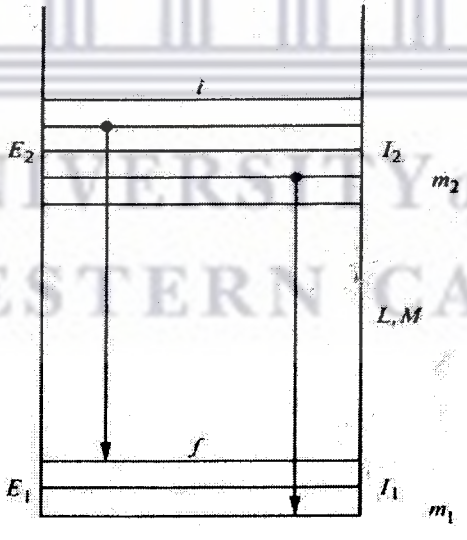

Figure 3.8: *The radiative line of multipolarity L between two nuclear levels of spin I_2 and I_1, each of which has 2I+ 1 substates characterized by the magnetic quantum number m [Bur79].*

The transition $I_2 \rightarrow I_1$ can have more than one multipolarity according to the selection rule,

$$I_i + I_f \geq L \geq |I_i - I_f| \qquad (7)$$

The electric multipole radiation of order L (L is the angular momentum quantum number of the radiation) has opposite parity to that of the magnetic radiation of the same multipolarity L according to the parity selection rule. Electric multipole radiation of order L has parity $\pi_E = (-1)^L$ and magnetic multipole radiation of order L has parity $\pi_M = -(-1)^L = (-1)^{L+1}$ [Mar69]. In general, the angular distribution of multipole radiation can be written in the form of a polynomial in even powers of cosθ:

$$W(\theta) = 1 + \sum_{k=1}^{L} a_{2k} \cos^{2k} \theta \qquad (8)$$

is known generally that the angular distribution, $W(\theta)$ depends on the value of m_i and m_f:

$$W(\theta) = \sum_{m_i} p(m_i) W_{m_i \rightarrow m_f}(\theta) \qquad (9)$$

where $p(m_i)$ is the population of the initial substate, therefore the fraction of nuclei that occupies the substate. The angular distribution $W(\theta)$ of the transition will be anisotropic if the relative populations $P(m_i)$ of the angular momentum substates are unequal, that is, $P(m_i) = P(m_j)$.

In heavy-ion induced reactions, a Gaussian distribution of substates is formed with the P(m) given by

$$P(m) = \frac{\exp(-m^2 / 2\sigma^2)}{\sum_{m'=-j}^{j} \exp(-m'^2 / 2\sigma^2)}$$

Here σ represents the width of the substate distribution.

3.7 Angular Correlations

Anisotropic angular correlations can be observed when we detect 2 γ-rays from a cascade even when P(m)=P(m′) because detecting the first γ-ray selects a certain substate population. Although in heavy ion reaction, oriented excited states are produced angular correlations could be applied.

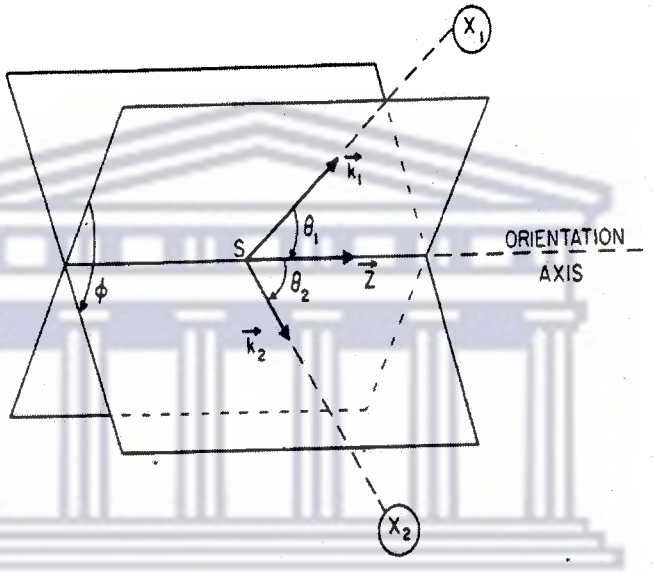

Figure 3.9: *The angles in a directional correlation of two successive radiations X_1 and X_2 emitted from an axial symmetric oriented source [Kra73].*

By measuring the angular correlation of two gamma rays emitted from oriented states, information about the multipolarity of transitions can be found. In order to determine the angular correlation, the two detectors are placed at an angle $\phi=\phi_1-\phi_2$ from each other, as shown in Fig 3.9, with the beam travelling along the z axis. We can express the intensity (the correlation function) with respect to their angles $W(\theta_1,\theta_2,\phi)$ as

$$W(\theta_1,\theta_2,\phi) = \sum_{\lambda_1\lambda\lambda_2} Q_k B_{\lambda 1}(I_1) A_\lambda^{\lambda_2\lambda_1}(X_1) A_{\lambda_2}(X_2) H_{\lambda_1\lambda\lambda_2}(\theta_1,\theta_2,\phi) \quad (10)$$

The $B_\lambda(I_1)$ are the orientation parameters, which depend on the substate population parameters and k indicate the direction of the successive radiations with respect to angle θ on the oriented axis:

$$B_\lambda(I_1) = (2I_1+1)^{\frac{1}{2}} \sum_m (-1)^{I_1+m} < I_1 - mI_1 m / \lambda 0 > P(m) \qquad (11)$$

The $A_\lambda^{\lambda_2\lambda_1}$ coefficients contain information on the nuclear wavefunction, and they depend on the mixing ratio $\delta = \frac{< I_3 \| \lambda' \| I_2 >}{< I_3 \| \lambda \| I_2 >}$, if a second transition in the cascade is mixed.

$$A_\lambda^{\lambda_2\lambda_1}(\delta) = \left[F_\lambda^{\lambda_2\lambda_1}(LLI_2I_1) + 2\delta F_\lambda^{\lambda_2\lambda_1}(LL'I_2I_1) + \delta^2 F_\lambda^{\lambda_2\lambda_1}(L'L'I_2I_1)\}\right] \frac{1}{1+\delta^2} \qquad (12)$$

The F-coefficients are products of Wigner 3-j and 9-j symbols. Finally the angular dependencies are contained in the $H_{\lambda\lambda_1\lambda_2}(\theta_1\theta_2\phi)$ coefficients, which are linear combinations of a product of spherical harmonics [Kra73].

The role of the Q_k is to correct all geometric effects on the observed distribution function, including finite source as well as finite detector size [Kra72]. The Q_k value depends on the energy of a given gamma ray and also depends on the size, and shape of the detector and its distance from the source. The Q_k values that have been used have been estimated by referring to the previous paper written by K.S Krane [Kra72]. In order to determine these values, we first measured the source-to-detector distance (194.5mm) in the AFRODITE array at iThemba LABS as depicted in the Fig 3.10. This distance was used to read out the Q_k values from Fig 3.11.

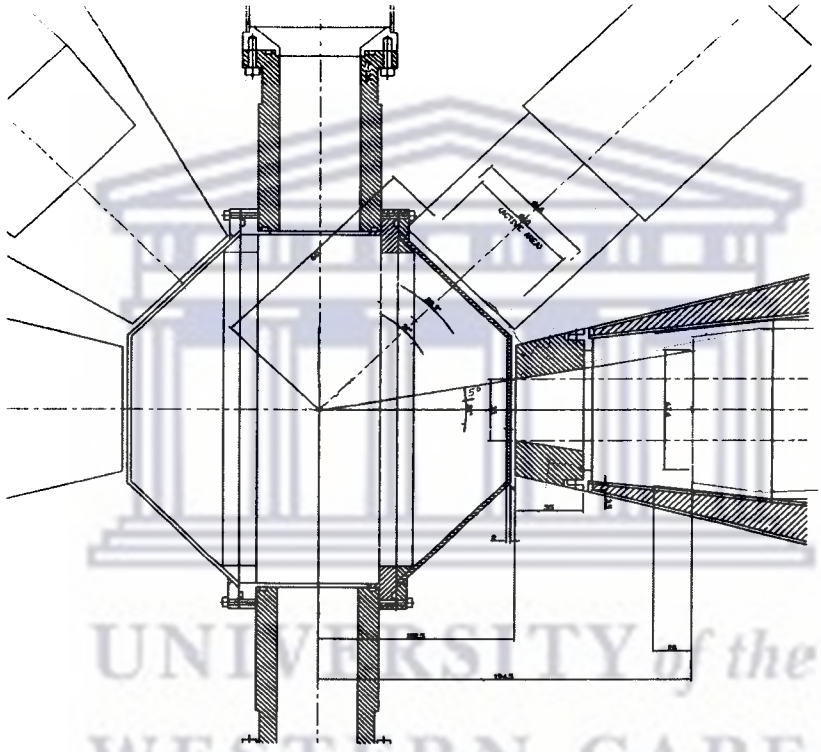

Figure 3.10: *The AFRODITE array detectors [Afr05].*

These Q_k values that are read out from Fig 3.11 by using source–to-detector distance are as follows, $Q_1 = 0.99$, $Q_2 = 0.98$, $Q_3 = 0.96$ and $Q_4 = 0.93$.

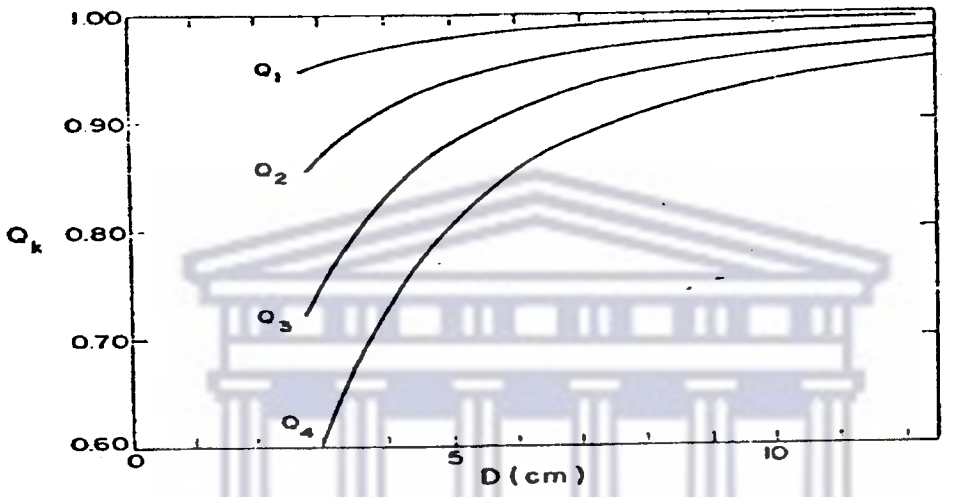

Figure 3.11: *Dependence of Q_k on source-to-detector distance [Kra72]*

3.8 DCO ratios for the geometry of AFRODITE

A by product of the recording of γ-γ coincidence data with AFRODITE is the angular correlations between the detectors. By gating on one transition, cleaner spectra are obtained with no other interference of some other transition which doesn't correlate with gated transition. However, to obtain the necessary statistics, it is usual to sum coincidences between detectors at the same angles and then to form a ratio, which minimizes uncertainties due to the efficiency calibration that have been made. Such ratios are called DCO (Directional Corrections from Oriented states) ratios. They are useful because by knowing them, we can sometimes distinguish between transitions of different multipolarities and also determine mixing ratios. The detectors of the AFRODITE array

are placed in rings at 135°(45°) and 90° with respect to the beam direction as shown in Fig 3.12. The DCO ratios were measured by constructing three different matrices; the first matrix consisted of the coincidences between detectors situated at 135°(y-axis) and 90° (x-axis). The projections of this two transpose matrices are shown in Fig 3.13 and Fig 3.14. Then the ratios of the γ-ray intensities are found by taking a gate on (135°-90°) and to (90°-135°) matrix:

$$R_{asym} = \frac{I(135° - 90°)}{I(90° - 135°)} \qquad (13)$$

Another two types of matrices were constructed "$135° - 135°$" and "$90° - 90°$", (with projections shown in Fig 3.15 and 3.16). The "135°-135°" matrix included only co-incidences between detectors placed at 135°, while the "90°-90°" matrix involved only coincidences between detectors at 90°. These matrices were used for determining the de-alignment parameter, σ / I by forming the following DCO ratio:

$$R_{sym} = \frac{I(135° - 135°)}{I(90° - 90°)} \qquad (14)$$

where $I(135° - 135°)$ and $I(90° - 90°)$ are the intensities of the peaks in the spectra gated on 135° and 90° detector respectively. The matrix was gated on time and the background subtraction was made by using a special programme called GF3.

The experimental DCO ratios would then be compared with the DCO ratios calculated using the program DCOPLOT, for various combinations of I_i, I_f, L1, L2, δ and σ/l. The DCO ratios were calculated by individually calculating the angular correlation for each detector combination, summing them together and forming the average DCO ratio. This was necessary because the θ=90° detectors of AFRODITE are not placed symmetrically around the beam axis as shown in Fig 3.12. The angular correlation function can be expressed in terms of even powers of $\cos^{2k}\varphi$, the different ϕ`s reduce to ϕ=0, 45° and 90°. A number of detector combinations for these angles are listed in table 3.1. Due to the asymmetric placement of the θ=90° detectors, the angle ϕ=45° is the most frequent with

equal numbers (DCO ratios) at 0° and 90°. To an accuracy of a few percent it was found that $W(\theta_1, \theta_2, 135°)$ could be used to calculate the DCO ratios for AFRODITE, which can be seen for example by comparing Fig 3.17 with Fig 3.18.

Table 3.1

Example of a few detectors combinations situated in different angles which have been used to calculate the DCO ratios,

Energy	Detectors	θ_1	ϕ_1	Energy		θ_2	ϕ_2	$\phi = \lvert \phi_2 - \phi_1 \rvert$
γ_1	C1	135	0	γ_2	C8	90	315	135
γ_1	C8	90	315	γ_2	C1	135	0	135
γ_1	C1	135	0	γ_2	C7	90	270	90
γ_1	C7	90	270	γ_2	C1	135	0	90
γ_1	C1	135	0	γ_2	C6	90	225	135
γ_1	C5	90	180	γ_2	C2	135	90	90

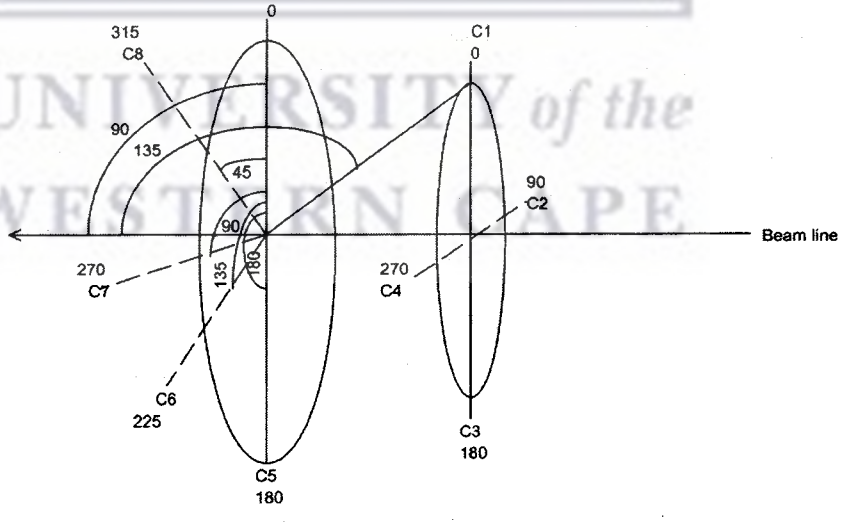

Figure 3.12: *Illustrating how the detectors are arranged in the AFRODITE array at iThemba LABS. C1 to C8 represent clover detectors 5 from 1 to 8.*

Figure 3.13 to Figure 3.16 represents the spectra for the matrices that have been created by using different angles of the clover detectors.

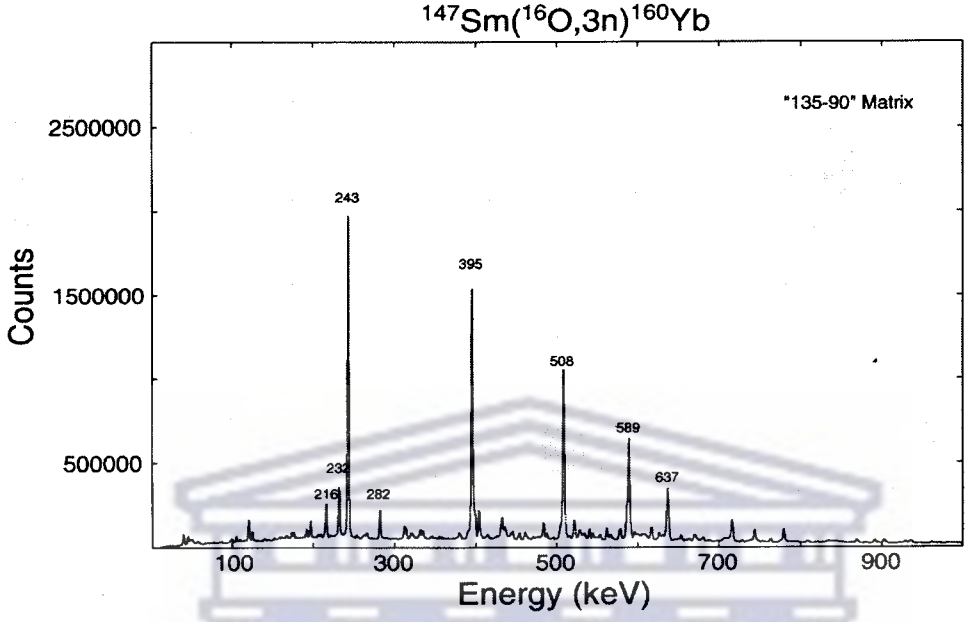

Figure 3.13: *The total projection spectrum for the "135-90" matrix. The matrix for γ-coincidence were created from two clover detectors situated at angle 135° and 90° with respect to beam direction.*

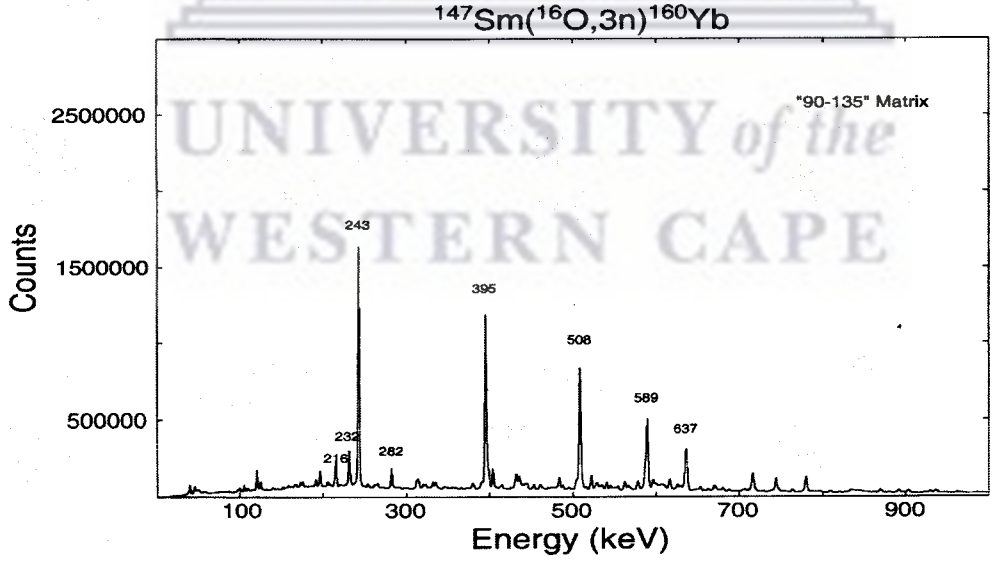

Figure 3.14: *This is the total projection spectrum for the "90-135" matrix. This is the transposed matrix for "135-90" matrix when the detector placed at 135°(y-axis) and 90°(x-axis) with respect to beam direction.*

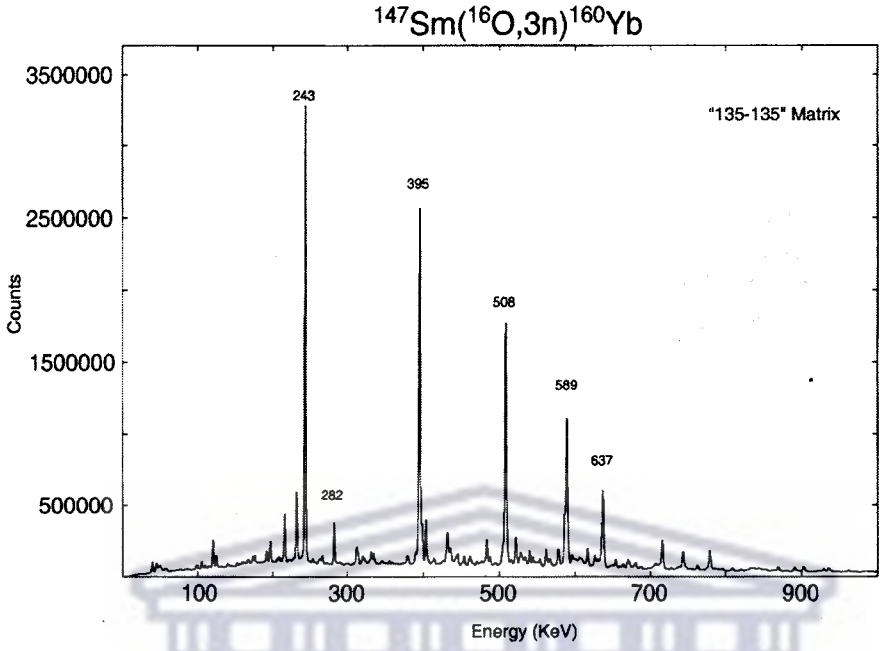

Figure 3.15: *The total projection spectrum for the "135-135" matrix.*

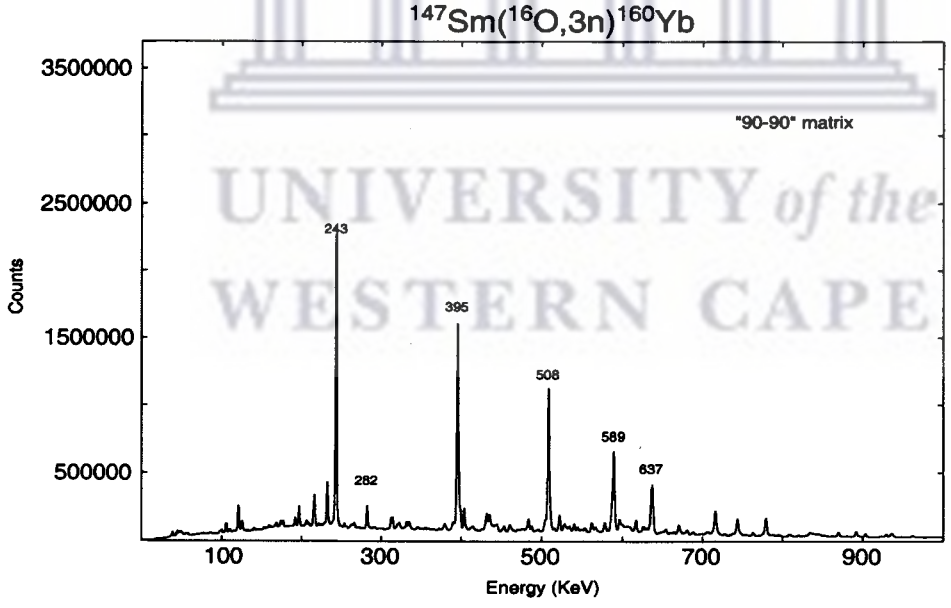

Figure 3.16: *The total projection spectrum for the "90-90" matrix.*

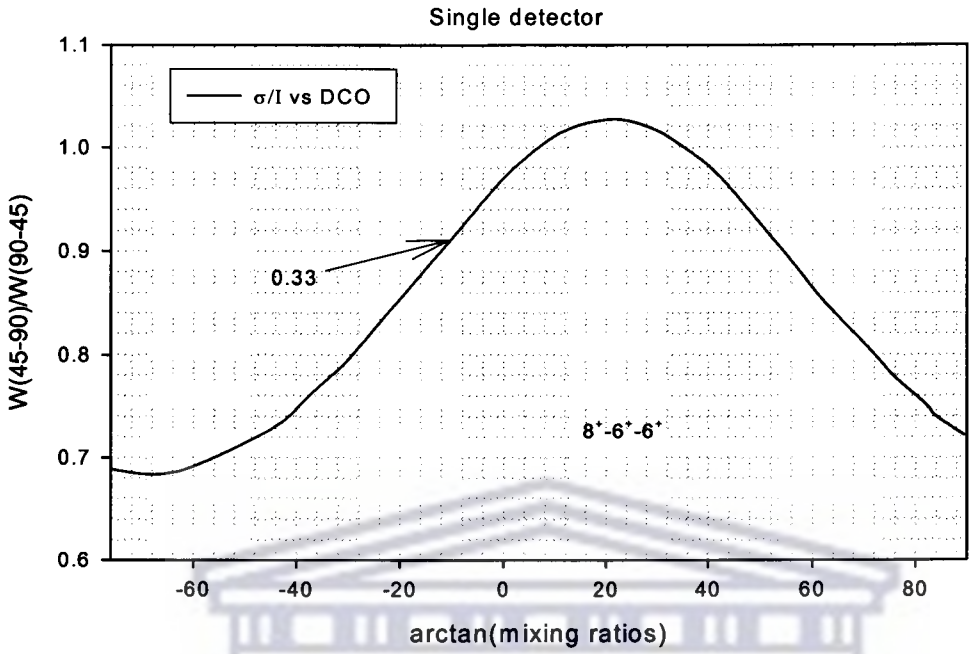

Figure 3.17: *Calculated DCO ratios, R_{DCO}=W(135-90)/W(90-135), as a function of arctan (δ) for σ/I=0.33. This diagram is for one detector combination correspond to W(135,90,135).*

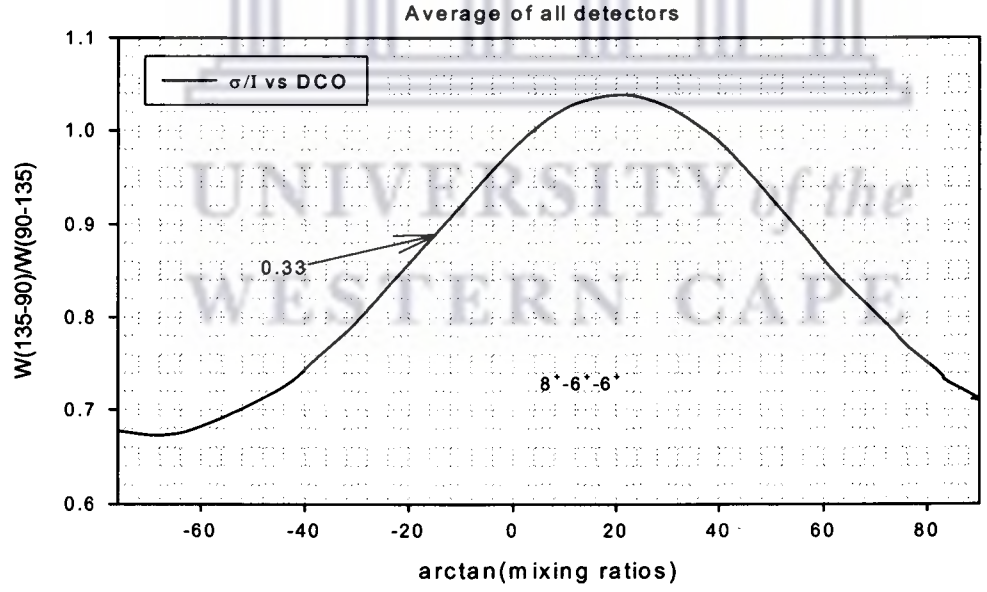

Figure 3.18: *Calculated DCO ratios, R_{DCO}=W(135-90)/W(90-135), as a function of arctan (δ) for σ/I=0.33. This diagram represents the average DCO ratio for all combinations of detectors for AFRODITE array.*

In Fig 3.19 calculated ratios of the correlation function for the two symmetrical geometries, W(135-135) and W(90-90) the angular correlations, are presented as a function of σ/I for different quadrupole cascades I→I-2→I-4.

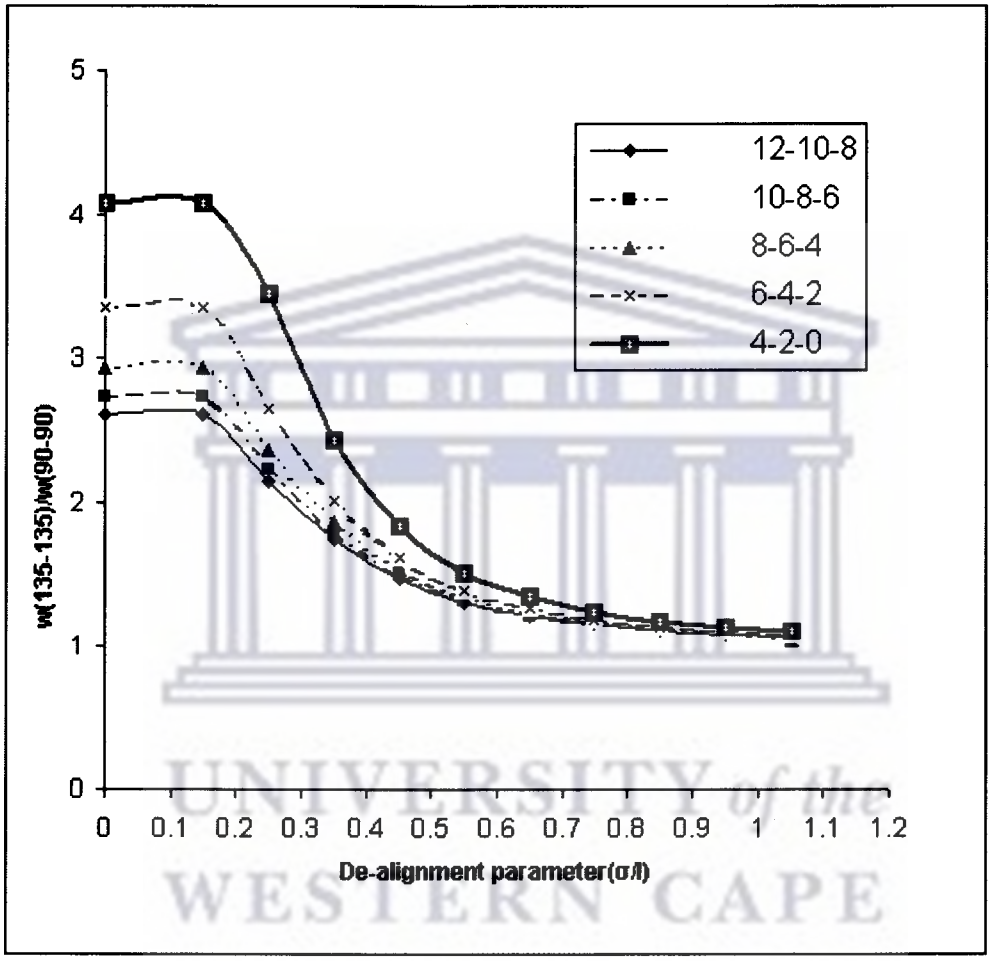

Figure 3.19: *Calculated ratios, W(135-135)/W(90-90), as a function of σ/I for different quadrupole cascades I→I−2→I−4.*

Thus a measurement of W(135°-135°)/W(90°-90°) allows σ/I to be read off these curves. Using the experimental values of R_{asym} obtained by gating on the strong transitions of the ground state band, the dependence of σ/I as a function of spin was determined, as shown

in Fig 3. 20. These values of σ/I were then used in the calculations of R_{asym}. Some examples are shown in Fig 3.21 to 3. 24 where the DCO ratios are calculated as a function of the mixing ratio for various combinations of spin and σ / I.

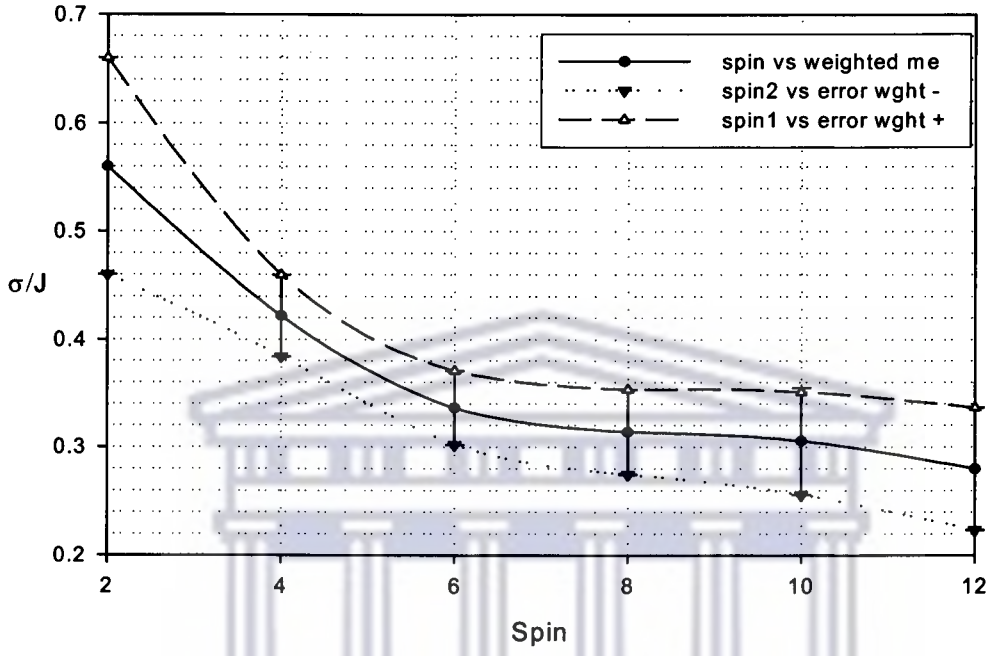

***Figure 3.20**: Illustrating the average spins from different bands in the level scheme of ^{160}Yb.*

Table 3.2

This table shows the calculated DCO ratios for a few different combinations of pure ML transitions.

Cascade	ML1	ML2	DCO
7–5–4	2	1	0.58
8–6–6	2	1	0.72
9–7–6	2	1	0.95
4–2–2	2	1	0.77

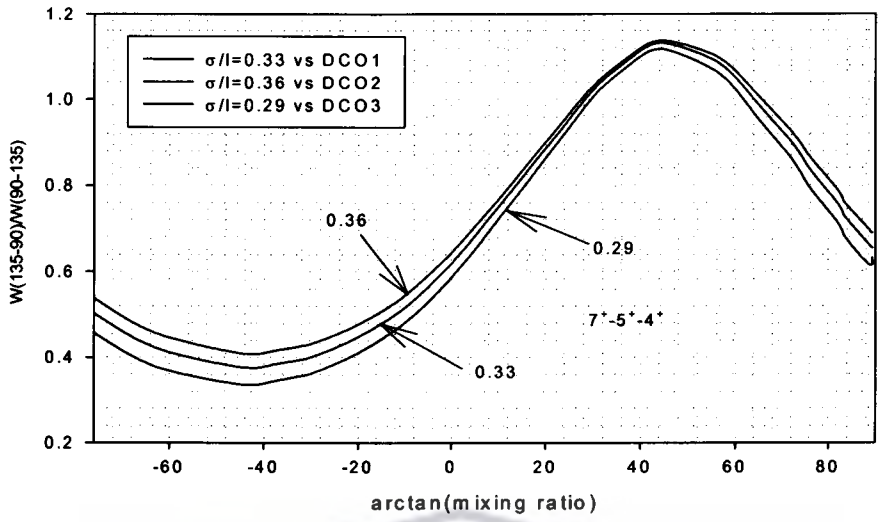

Figure 3.21: *Calculated DCO ratios, R_{asym}=W(135-90)/W(90-135), as a function of arctan(δ) for different values of σ/I. The DCO1, DCO2 and DCO3 indicate the DCO ratios of each curve on the y axes.*

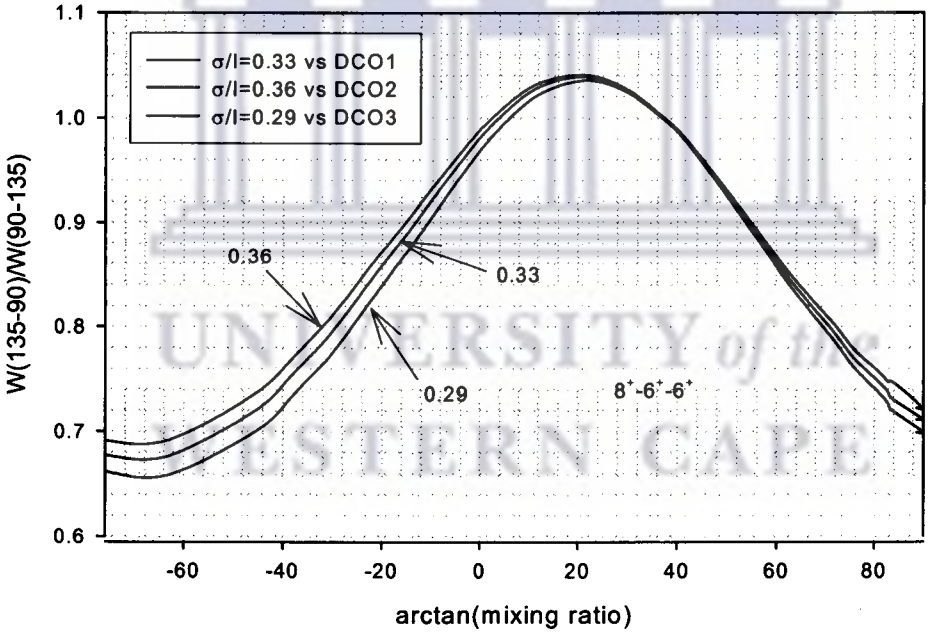

Figure 3.22: *Calculated DCO ratios, R_{asym}=W(135-90)/W(90-135), as a function of arctan(δ) for different values of σ/I. The DCO1, DCO2 and DCO3 indicate the DCO ratios of each curve on the y axes.*

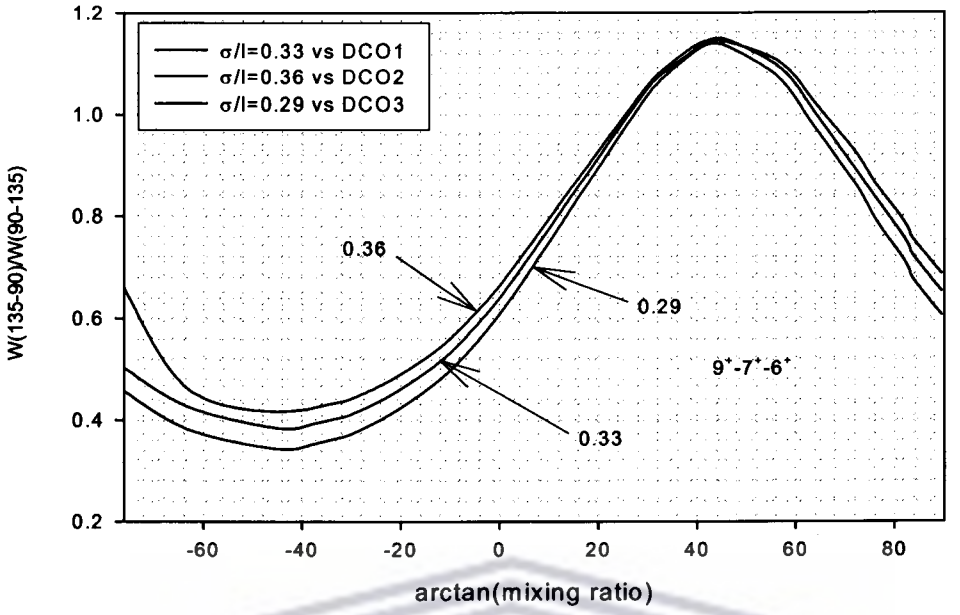

Figure 3.23: *Calculated DCO ratios, R_{asym}=W(135-90)/W(90-135), as a function of arctan(δ) for different values of σ/I. The DCO1, DCO2 and DCO3 indicate the DCO ratios of each curve on the y axes.*

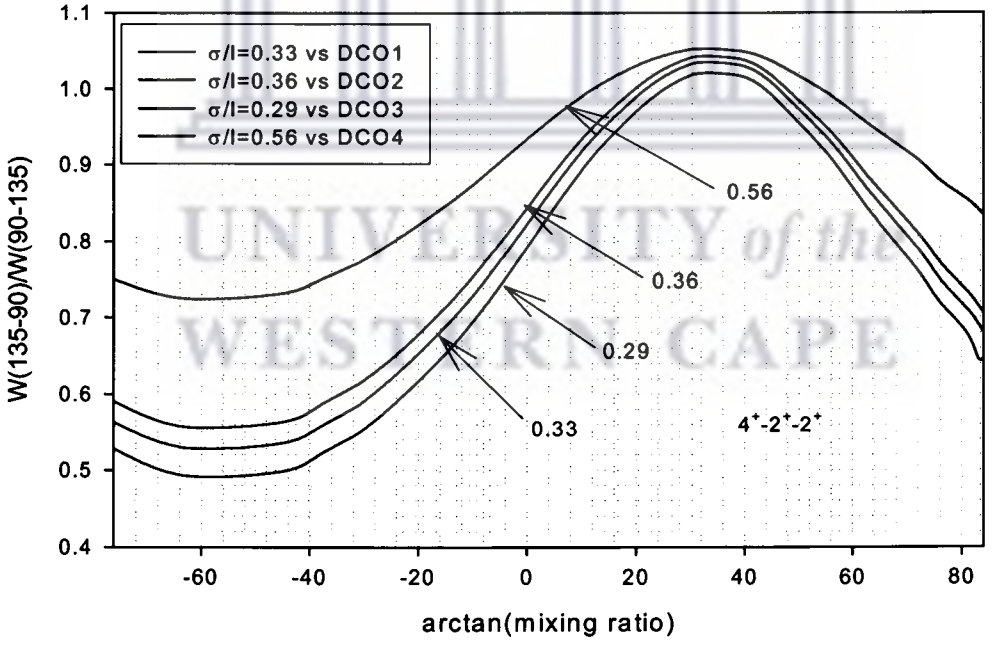

Figure 3.24: *Calculated DCO ratios, R_{asym}=W(135-90)/W(90-135), as a function of arctan(δ) for different values of σ/I. The DCO1, DCO2, DCO3 and DCO4 indicate the DCO ratios of each curve on the y axes.*

3.9 Mixing ratios

The mixing ratios were obtained for some transitions in the constructed level scheme of ^{160}Yb. As an example we used a plot such as that shown in Fig 3.25 to determine the mixing ratios. The measured DCO ratio (y-axes) was used during the determination of mixing ratio. We read out the values of the mixing ratios on the x-axis as depicted from the figure.

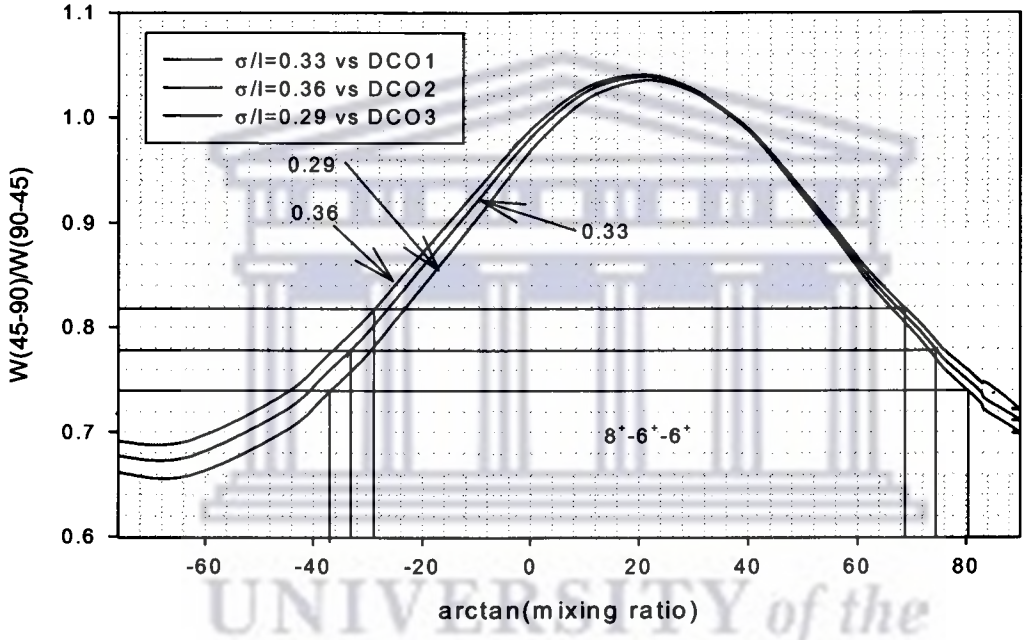

Figure 3.25: *Calculated DCO ratios, R_{DCO}=W(135-90)/W(90-135), as a function of arctan(δ) for different values of σ/I*

In general, one sees that there is an ambiguity in the mixing ratio obtained from a measurement of R_{asym}- usually two values are possible, and additional information is required to choose between the two.

CHAPTER 4

Results of data analysis

The level scheme of ^{160}Yb, deduced in the present work is shown in Fig 4.1. Gamma-ray energies, intensities and DCO ratios are listed in table 4.1. Bands are labelled as band 1 to 12. The previous level schemes [Byr87], [Rie80], [Aue84] and [Gar82], from β-decay and the (^{16}O, 3n) reaction are shown in Fig 4.2 to 4.5. Several new bands have been added, such as bands 7 to 12. However, the present level scheme does not extend to as high a spin as that of Byrski et al [Byr87] shown in Fig 4.2. This of course, is due to the use of a thick target, which has caused the states at high spin to be Doppler broadened. The β-decay work had already identified some of the low-lying levels of bands 1, 3 and 6-8. However, there are some conflicts with the spin and parity assignments of the present work and that of Auer et al. [Aue84].

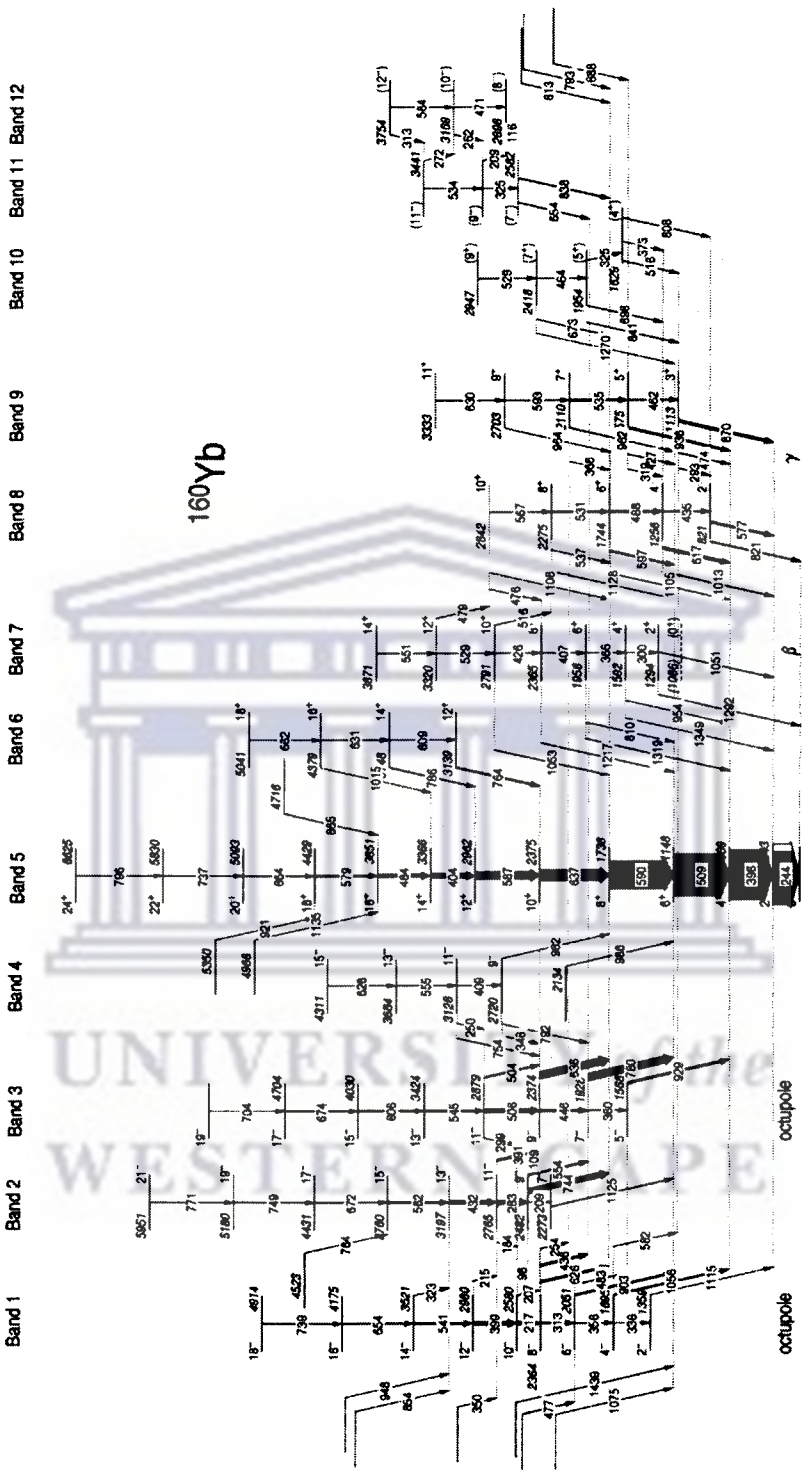

Figure 4.1: *Level scheme of ^{160}Yb with new additional bands.*

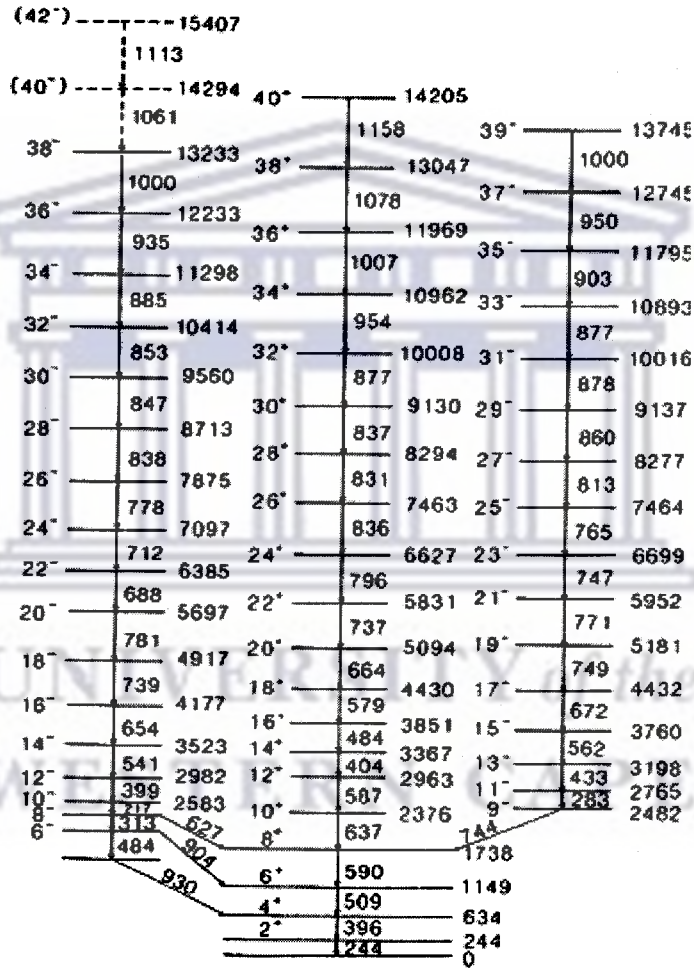

Figure 4.2: *Level scheme of ^{160}Yb [Byr87]*

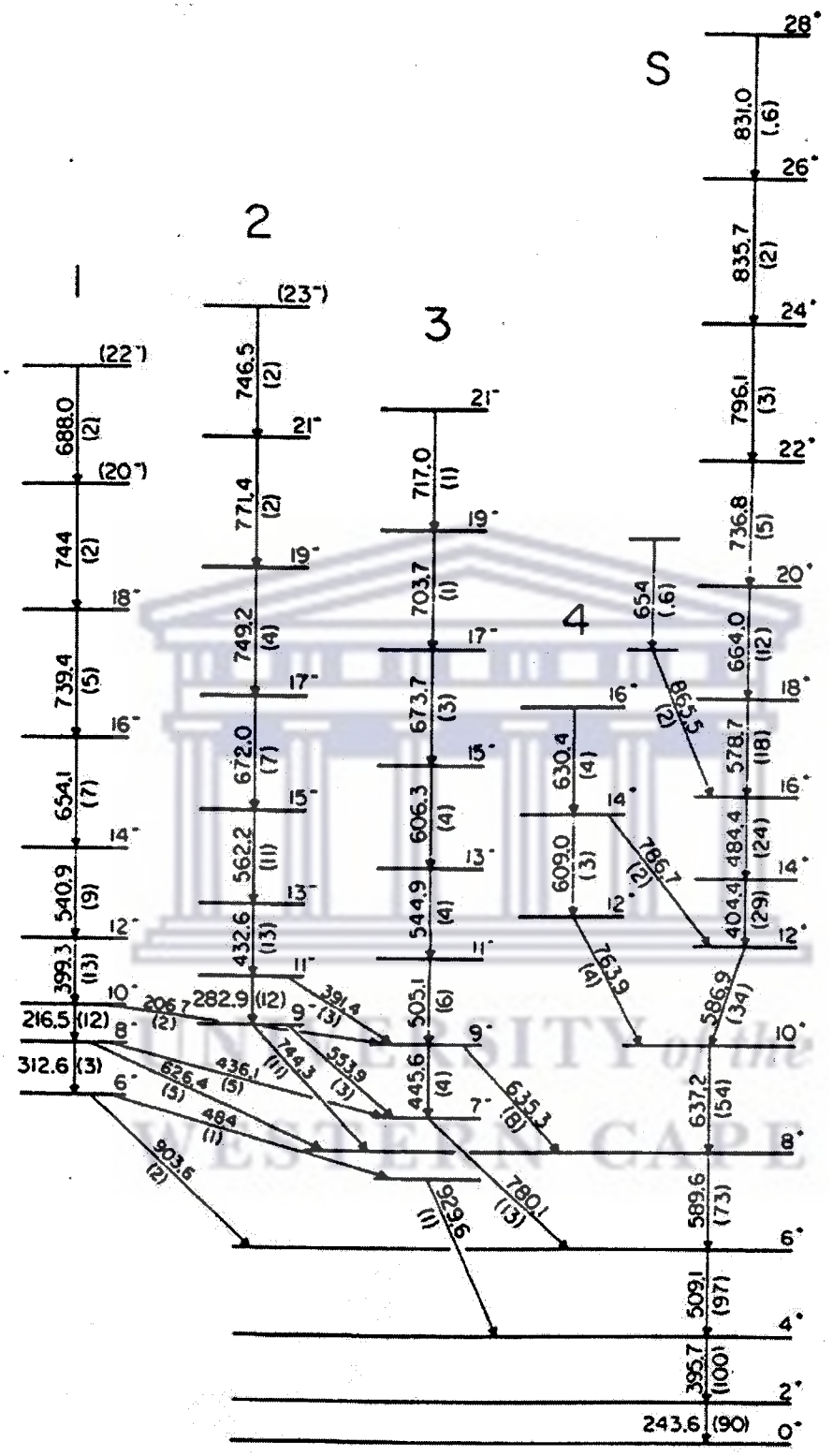

Figure 4.3: *The Level scheme of ^{160}Yb from (^{16}O, 3n) measurements of [Rie80]*

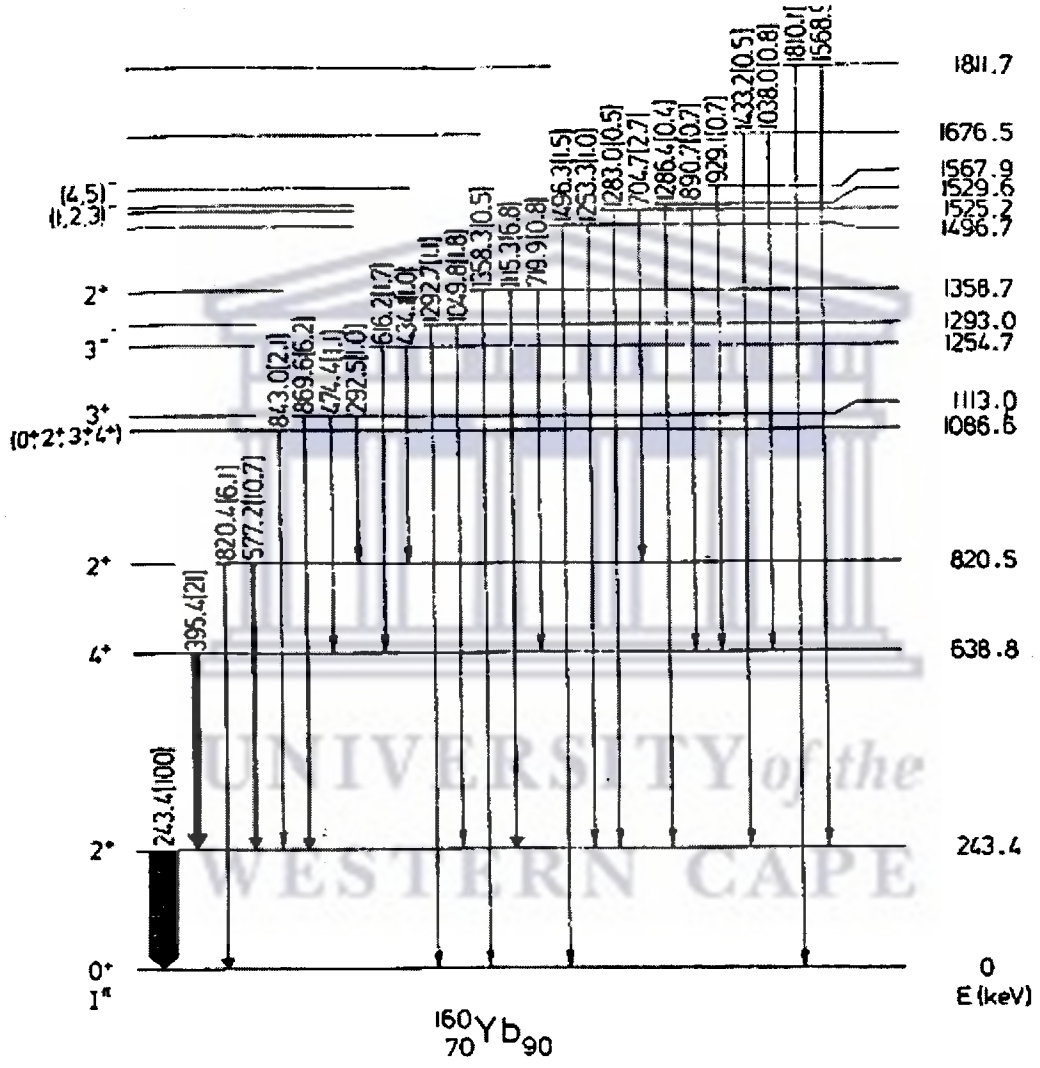

Figure 4.4: *The decay scheme of ^{160}Yb, where the intensities are normalized to I(243 keV)=100 from ß-decay work of [Aue84].*

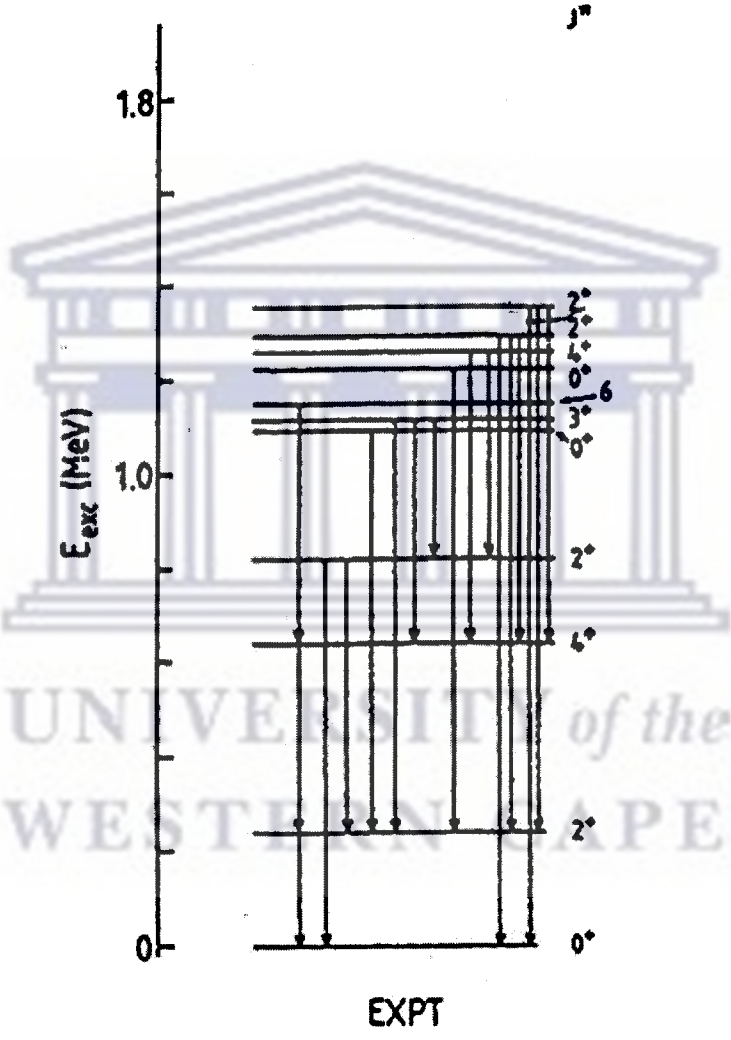

Figure 4.5: *Experimental level schemes for ^{160}Yb from the ß-decay work of Garret et al [Gar82].*

Table 4.1

This table indicates the gamma-ray energies (E_γ), intensities (I_γ), DCO ratios, and mixing ratios δ which have been measured. The gate was almost taken on stretched E2 transition.

E_γ (keV)	I_γ	E_i (keV)	E_f (keV)	$J_i(\hbar)$	$J_f(\hbar)$	*DCO*	δ
98.37(4)	2.4(1)	2580.4(3)	2482.0	10-	9-		
108.73(6)	1.4(1)	2482.0(3)	2373.6	9-	9-		
115.78(3)	1.5(1)	2697.7(3)	2582.0	(8-)	(7-)		
184.47(6)	1.8(1)	2764.8(3)	2580.4	11-	10-		
206.82(3)	10.3(4)	2580.4(3)	2373.6	10-	9-		
209.06(10)	1.0(1)	2482.0(3)	2272.9	9-	7-	1.05(11)	
209.28(3)	4.0(2)	2906.9(3)	2697.7	(9-)	(8-)		
214.90(4)	4.1(2)	2979.8(3)	2764.8	12-	11-	1.00(8)	
216.56(3)	63.7(20)	2580.4(3)	2364.0	10-	8-	0.90(7)	
243.50(3)	56.9(57)	243.50(3)	0.0	2+	0+	0.97(7)	
249.59(5)	2.6(2)	3128.3(3)	2879.1	11-	11-		
254.09(3)	9.7(3)	2364.0(2)	2110.0	8-	7+	0.57(6)	
261.96(4)	3.1(1)	3168.9(3)	2906.9	(10-)	(9-)		
271.92(4)	1.7(1)	3440.7(3)	3168.9	(11-)	(10-)		
282.89(3)	80.1(25)	2764.8(3)	2482.0	11-	9-	1.14(9)	
292.62(4)	4.1(2)	1113.3(2)	820.7	3+	2+	0.69(8)	
298.67(10)	1.2(3)	2879.1(3)	2580.4	11-	10-		
299.54(21)	0.4(1)	1592.4(3)	1293.7	4+	2+		
312.58(3)	24.7(8)	2364.0(2)	2051.3	8-	6-	0.99(8)	
313.29(5)	2.0(1)	3753.7(4)	3440.7	(12-)	(11-)		
319.38(5)	2.8(11)	1575.1(2)	1256.0	5+	4+		
323.46(5)	2.8(1)	3520.7(3)	3197.2	14-	13-		
324.71(5)	1.9(1)	2906.9(3)	2582.0	(9-)	(7-)		
325.21(5)	3.8(2)	1954.3(3)	1629.1	(5+)	(4+)	0.57(6)	
336.44(9)	1.4(4)	1695.4(3)	1358.9	4-	2-		
346.29(4)	9.1(5)	2719.9(3)	2373.6	9-	9-	0.98(13)	
349.90(6)	2.7(2)	3114. 7(4)	2764.8	13-	11-		
355.99(4)	8.7(4)	2051.3(2)	1695.4	6-	4-	1.10(10)	
359.60(4)	6.2(5)	1928.0(2)	1568.4	7-	5-	1.00(11)	
365.85(6)	2.9(2)	1958.2(3)	1592.4	6+	4+	1.10(18)	
366.03(6)	1.9(1)	2110.0(2)	1744.4	7+	6+		
373.20(9)	2.3(2)	1629.1(2)	1256.0	(4+)	4+	1.18(10)	
391.10(3)	36.2(12)	2764.8(3)	2373.6	11-	9-	0.88(7)	
395.69(3)	1000.0(301)	639.1(2)	243.3	4+	2+	0.93(7)	
399.38(3)	74.2(23)	2979.8(3)	2580.4	12-	10-	1.13(9)	
404.32(3)	100.4(30)	3366.1(3)	2961.9	14+	12+	1.00(8)	
407.12(4)	8.3(3)	2365.4(3)	1958.2	8+	6+	1.20(11)	
408.53(5)	3.2(2)	3128.3(3)	2719.9	(11-)	(9-)	1.03(14)	
425.83(5)	4.8(2)	2791.2(3)	2365.4	10+	8+	0.80(9)	
427.38(5)	6.0(3)	1575.1(2)	1148.0	5+	6+	0.98(10)	

E_γ (keV)	I_γ	E_i (keV)	E_f (keV)	$J_i(\hbar)$	$J_f(\hbar)$	*DCO*	δ
432.42(3)	75.6(23)	3197.2(3)	2764.8	13	11	1.17(10)	
435.41(3)	21.2(7)	1256.0(2)	820.7	4+	2+	1.02(9)	
435.97(3)	36.0(12)	2364.0(2)	1928.0	8-	7-	0.47(4)	
445.64(3)	38.1(14)	2373.6(3)	1928.0	9-	7-	1.16(10)	
461.61 (3)	28.6(9)	1575.1(2)	1113.3	5+	3+	1.02(12)	
463. 76(4)	7.4(3)	2418.0(3)	1954.3	(7+)	(5+)	0.91(8)	
471.19(5)	3.0(2)	3168.9(3)	2697.7	(10-)	(8-)		
474.39(5)	7.4(4)	1113.3(2)	639.1	3+	4+	0.72(7)	
476.46(6)	4.1(2)	2841.9(3)	2365.4	10+	8+		
477.41(4)	11.7(5)	2528.7(3)	2051.3		6-		
478.61(6)	3.8(2)	3320.3(3)	2841.9	12+	10+	0.68(7)	
482.92(4)	10.9(4)	2051.3(2)	1568.4	6-	5-	0.75(8)	
484.37(3)	65.7(20)	3850.5(3)	3366.1	16+	14+	1.01(8)	
488.32(3)	40.9(13)	1744.4(2)	1256.0	6+	4+	0.99(9)	
503.73(3)	23.0(11)	2879.1(3)	2375.1	11-	10+	0.93(8)	
505.73(3)	75.6(26)	2879.1(3)	2373.6	11-	9-		
509.05(3)	858.8(258)	1148.0(2)	639.1	6+	4+	0.97(8	
515.78(5)	7.4(4)	1629.1(2)	1113.3	(4+)	3+	0.66(11	
515.86(5)	5.4(2)	2791.2(3)	2275.4	10+	8+	0.92(8)	
529.01(4)	11.4(4)	3320.3(3)	2791.2	12+	10+	0.98(9)	
529.06(5)	7.6(3)	2947.1(4)	2418.0	(9+)	(7+)		
531.18(3)	27.2(9)	2275.4(3)	1744.4	8+	6+	1.15(10)	
533.93(5)	3.4(2)	3440.7(3)	2906.9	(11-)	(9-)		
534.90(3)	38.5(12)	2110.0(2)	1575.1	7+	5+	1.09(10)	
537.12(8)	5.4(4)	2275.4(3)	1737.6	8+	8+		
540.88(3)	43.8(14)	3520.7(3)	2979.8	14-	12-	1.02(8))	
545.03(3)	31.6(12)	3424.1(3)	2879.1	13-	11-	1.04(9)	
550.99(4)	7.0(3)	3871.3(4)	3320.3	14+	12+		
553.92(3)	24.8(9)	2482.0(3)	1928.0	9-	7-	1.02(9	
555.33(5)	6.0(3)	3683.6(4)	3128.3	13-	11-		
562.28(3)	39.8(12)	3759.5(3)	3197.2	15-	13-		
566.59(4)	10.4(4)	2841.9(3)	2275.4	10+	8+		
577.41(3)	32.9(12)	820.7(2)	243.3	2+	2+	0.77(6)	$\delta < -0.1; \delta > 3$
578.54(3)	35.1(11)	4429.1(4)	3850.5	18+	16+	0.98(8)	
582.44(9)	2.6(3)	1695.4(3)	1113.3	4-	3+		
584.45(6)	3.2(2)	3753.7(4)	3168.9	(12-)	(10-)		
586.80(3)	156.4(47)	2961.9(3)	2375.1	12+	10+	0.89(7)	
589.56(3)	576.3(173)	1737.6(2)	148.0	8+	6+	1.11(9)	
592.78(4)	16.8(6)	2702.7(3)	2110.0	9+	7+	1.11(11)	
596.59(4)	26.0(9)	1744.4(2)	1148.0	6+	6+	0.72(6)	$\delta < -0.7; \ \delta > 29$

E_γ (keV)	I_γ	E_i (keV)	E_f (keV)	$J_i(\hbar)$	$J_f(\hbar)$	DCO	δ
606.02(3)	18.5(7)	4030.1(3)	3424.1	15-	13-	1.05(9)	
609.35(4)	8.6(4)	3748.4(3)	3139.0	14+	12+	0.86(9)	
616.98(3)	49.9(18)	1256.0(2)	639.1	4+	4+	0.78(7)	$\delta < -0.6$; $\delta > 7$
626.34(3)	37.3(13)	2364.0(2)	1737.6	8-	8+	1.01(8)	
627.63(6)	3.8(2)	4311.3(4)	3683.6	15-	13-		
629.93(4)	8.7(3)	3332.7(3)	2702.7	11+	9+	0.41(6)	
630.84(4)	12.4(5)	4379.4(3)	3748.4	16+	14+		
636.22(3)	145.6(60)	2373.6(3)	1737.6	9-	8+		
637.31(3)	230.1(69)	2375.1(3)	1737.6	10+	8+	0.89(7)	
654.08(3)	22.4(7)	4174.8(3)	3520.7	16-	14-	0.93(8)	
654.14(5)	7.7(4)	2582.0(3)	1928.0	(7-)	7-		
661.91(9)	2.3(2)	5041.3(5)	4379.4	18+	16+		
663.86(3)	13.0(4)	5092.9(4)	4429.1	20+	18+		
671.76(3)	17.6(6)	4431.3(3)	3759.5	17-	15-		
673.23(9)	3.0(2)	2418.0(3)	1744.4	(7+)	6+		
673.60(4)	6.0(3)	4703.7(4)	4030.1	17-	15-	0.99(9)	
688.05(11)	2.8(1)	2263.1(5)	1575.1		5+		
698.40(5)	8.2(4)	1954.3(3)	1256.0	(5+)	4+	0.59(5)	
703.84(7)	2.2(2)	5407.6(5)	4703.7	19-	17-		
736.68(5)	4.2(2)	5829.6(4)	5092.9	22+	20+		
739.39(4)	8.6(3)	4914.2(4)	4174.8	18-	16-	0.97(9)	
744.34(3)	103.5(41)	2482.0(3)	1737.6	9-	8+	0.64(5)	
748.78(4)	8.1(3)	5180.1(4)	4431.3	19-	17-	0.55(5)	
754.05(6)	6.5(5)	3128.3(3)	2373.6	11-	9-	0.72(8)	
763.70(11)	1.7(1)	4523.2(6)	3759.5		15-		
763.83(3)	25.9(8)	3139.0(3)	2375.1	12+	10+		
771.14(7)	1.9(1).	5951.2(5)	5180.1	21-	19-		
779.93(3)	145.8(159)	1928.0(2)	1148.0	7-	6+	0.55(5)	
786.48(4)	13.1(6)	3748.4(3)	2961.9	14+	12+		
791.98(13)	2.3(2)	2719.9(3)	1928.0	9-	7-		
793.49(8)	3.3(1)	2537.9(4)	1744.4		6+		
795.89(6)	2.7(1)	6625.5(5)	5829.6	24+	22+		
808.40(6)	8.5(3)	1629.1(2)	820.7	(4+)	2+	1.05(13)	
810.17(10)	3.0(3)	1958.2(3)	1148.0	6+	6+	0.54(5)	
812.90(8)	4.2(2)	2557.3(4)	1744.4		6+		
820.70(5)	17.9(8)	820.7(2)	0.0	2+	0+	0.98(10)	
837.53(3)	14.7(6)	2582.0(3)	1744.4	(7-)	6+		
841.04(6)	6.5(3)	1954.3(3)	31113.3	5+	3+	0.68(8)	
854.00(9)	2.8(2)	4051.2(5)	3197.2		13-		
865.18(7)	3.1(2)	4715.7(5)	3850.5		16+		

E_γ (keV)	I_γ	E_i (keV)	E_f (keV)	$J_i(\hbar)$	$J_f(\hbar)$	*DCO*	δ
869.89(3)	47.7(26)	1113.3(2)	243.3	3+	2+	0.67(6)	$\delta < 0.2$; $\delta > 29$
903.30(3)	31.0(12)	2051.3(2)	1148.0	6-	6+	0.87(8)	
921.27(18)	0.9(1)	5350.3(9)	4429.1		18+		
929.32(4)	38.5(12)	1568.4(3)	639.1	5-	4+	0.67(6	
935.80(4)	35.7(13)	1575.1(2)	639.1	5+	4+	0.58(5)	$-19 < \delta < -2.0$; $-0.4 < \delta < 0.0$
947.80(21)	1.1(2)	4145.0(9)	3197.2		13-		
953.53(18)	1.3(4)	1592.4(3)	639.1	4+	4+	0.95(12)	
961.96(6)	8.9(4)	2110.0(2)	1148.0	7+	6+		
963.54(43)	1.0(3)	2702.7(3)	1737.6	9+	8+		
982.33(38)	1.3(7)	2719.9(3)	1737.6	9-	8+		
985.68(14)	5.1(3)	2133.7(7)	1148.0		6+		
1012.93(6)	10.3(5)	1256.0(2)	243.3	4+	2+	1.00(11)	
1015.00(15)	1. 7(2)	4379.4(3)	3366.1	16+	14+		
1050.95(17)	7.9(5)	1293.7(6)	243.3	2+	2+		
1053.46(6)	8.7(5)	2791.2(3)	1737.6	10+	8+	0.86(8)	
1056.27(5)	25.6(8)	1695.4(3)	639.1	4-	4+	1.12(11)	
1075.39(19)	3.8(3)	2223.4(9)	1148.0		6+		
1105.42(14)	5.1(4)	1744.4(2)	639.1	6+	4+		
1105.69(28)	1.9(4)	2841.9(3)	1737.6	10+	8+		
1115.36(17)	1.3(2)	1358.9(4)	243.3	2-	2+	0.46(8)	
1124.85(8)	9.1(4)	2272.9(4)	1148.0	7-	6+		
1127.52(20)	2.9(4)	2275.4(3)	1148.0	8+	6+	0.62(79)	
1135.49(16)	1.4(2)	4986.0(8)	3850.5		16+		
1217.16(8)	7.2(4)	2365.4(3)	1148.0	8+	6+	0.97(10)	
1269. 70(**41**)	1.2(2)	2418.0(3)	1148.0	(7+)	6+		
1292.48(140)	5.2(25)	1293.7(6)	0.0	2+	0+		
1319.02(7)	8.2(6)	1958.2(3)	639.1	6+	4+	0.92(9)	
1348.93(15)	2.4(8)	1592.4(3)	243.3	4+	2+		
1439.34(19)	4.6(3)	2587.3(9)	1148.0		6+		

4.1 γ - γ Coincidences

Gates showing transitions associated with the new bands in the level scheme depicted in Fig 4. 2 are shown in figures 4.6 and 4.7

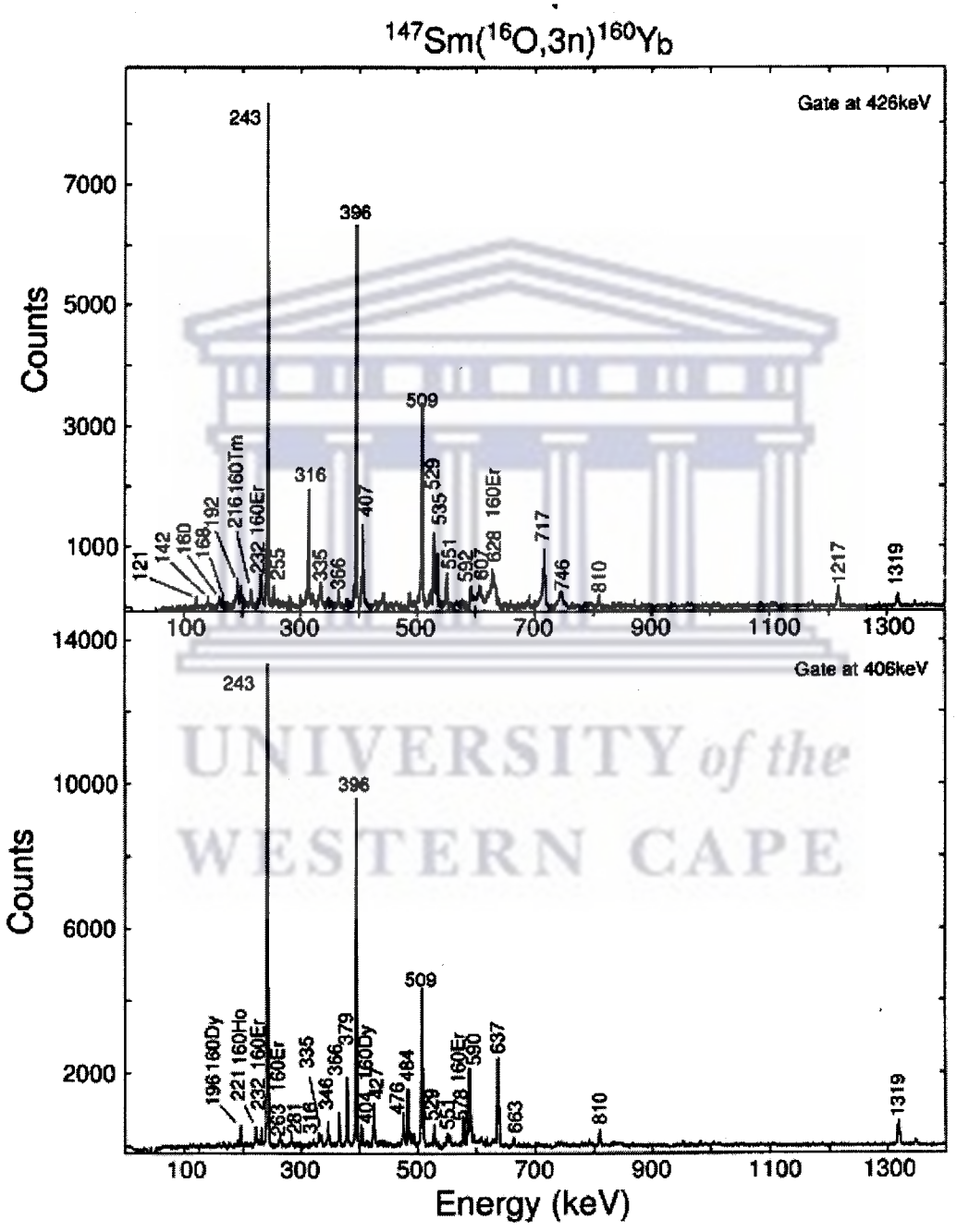

Figure 4.6: *The γ-ray coincidence spectra extracted from the gated matrix. Gates taken at 425 keV and 406 keV transitions from Band 7*

In order to get the coincidence spectra illustrated in Figure 4.6 and 4.7, gates were set on transitions subsequently placed in the constructed level scheme of ^{160}Yb. The gate at 426 keV (Fig 4.6) is taken from a transition in band 7 in the level scheme. In that case we can only see the transitions which are below and above the gated transition i.e. that follow the decay path of the gated transition. The transitions which are in the other bands and do not follow the decay path of the gated transition are not observed. In general, when taking gates on different transitions in the same band, the transitions that can be observed in the first gates must also be observed in the other gates, because those gates will follow the same decay path. The peaks labelled as ^{160}Er, ^{160}Tm etc, are from contaminating nuclei which are formed in the reaction. These appear in the spectrum because it is possible for a transition of the same energy to be present in different nuclei, or in the same nucleus but in different bands.

The gates taken at 929keV, 1319keV and 535keV have different decay paths, even though there are some other transitions that are linked together by crossing bands from one band to another. The transitions observed after taking a gate from one of the transitions in the bands are shown in Fig 4.7. All these transitions have different characteristics and multipolarities.

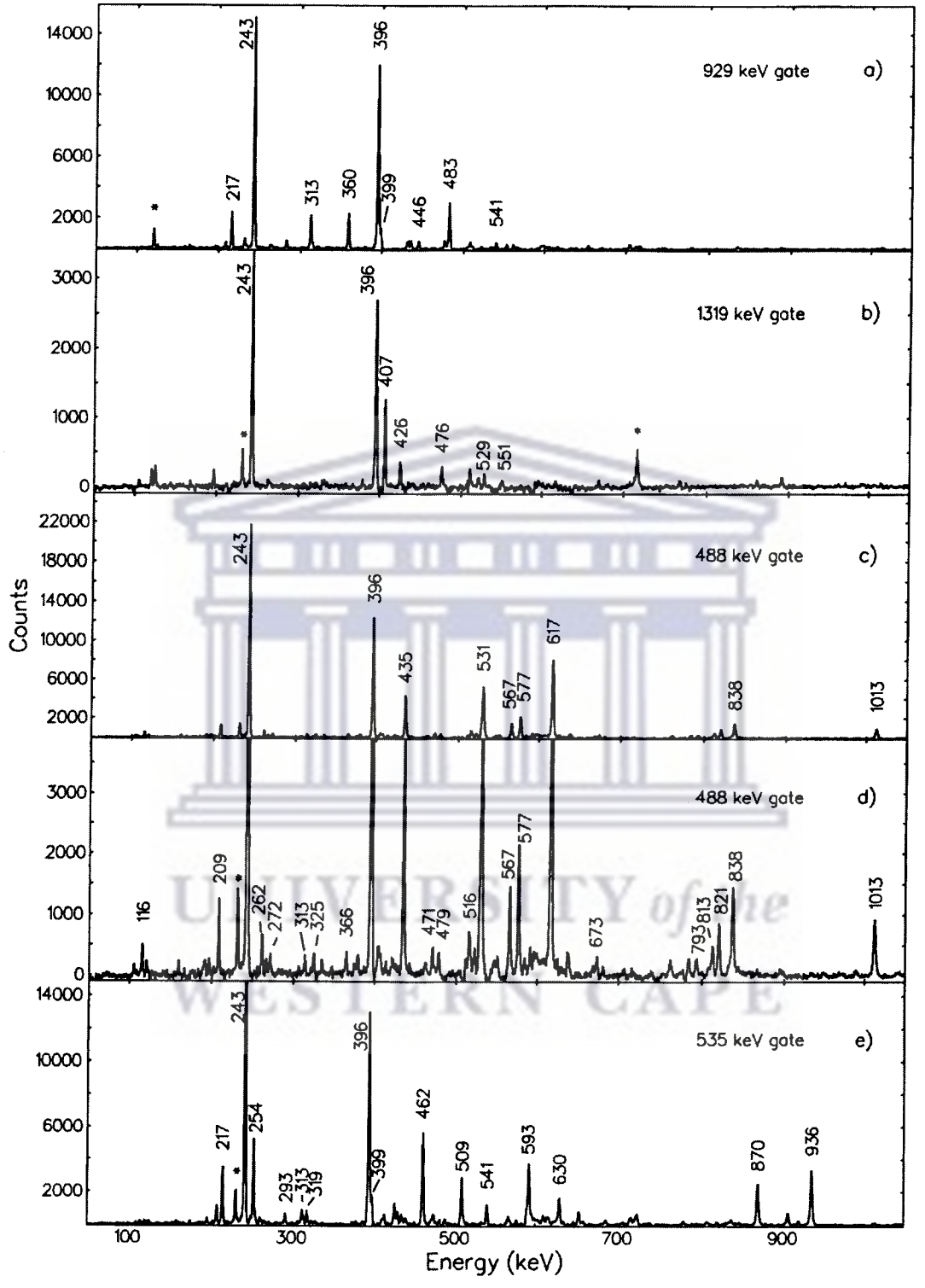

Figure 4.7: *The γ-ray coincidence spectra obtained from the time gated matrix. Gates were taken at 929 keV, 1319 keV, 488 keV, and 535 keV. The peaks labelled as * represent the interference of some other nucleus when the reaction takes place.*

4.2 Construction of level scheme

Bands 1 to 3 form a set of negative parity bands, which have been extended to lower spin in the present work. The placement of the level at 1568 keV, as the 5^- member of band 3 by Reidinger et al [Rie80] (see Fig 4.3) is now confirmed with a connection to the 7^- level via a transition of 360 keV, as shown in the 929 keV coincidence gate of Fig 4. 7a. Band 1 is instead now extended down to the 2^- level, first reported by Garret et al [Gar82], at 1359 keV. Finally, Band 2 is extended to a 7^- state with the placement of a 209 keV transition in the band, and by its decay to the ground band via a transition of 1125 keV energy.

Beta-decay work has established numerous levels at low spin in ^{160}Yb. In particular, levels at 821 and 1113 keV were assigned to the 2^+ and 3^+ members of the gamma band [Aue85] (see Fig 4.4). The gamma band is now extended to spin 11, with the observation of Bands 8 and 9. Spectra demonstrating the existence of these bands are shown in Fig 4. 7c-e. However, the level at 1256 keV in Band 8, was assigned spin and parity of 3^- by Auer et al [Aue84], based on measured conversion coefficients for the 617 and 435 keV transitions. This assignment is rejected here because our DCO ratio for the 435 keV transition, 1.02(9) is inconsistent with stretched E1, and if a 3^- assignment were adopted, M2 multipolarity would be required for the 319 and 366 keV transition linking band 8 to band 9. Limits on mixing ratios have been extracted for some of the transitions depopulating the levels in these bands to the ground state band. In particular, those for the 577 and 870 keV transitions are consistent with the pure E2 assignment favoured in the angular correlation analysis of Garret et al [Gar82], and therefore we adopt this alternative from our analysis. Visible in Fig 4.7d are the 516 and 479 keV transitions, which link band 7 to band 8. Apparently, these transitions, and the 476 keV transition from band 8 to band 7, are the result of mixing due to the chance degeneracy of levels at 2791 and 2842 keV. On this basis the 2791 keV level of band 7 is assigned as a 10^+ state, which in turn fixes the spins and parities of all the members of band 7, which is observed down to the 2^+ state. Members of band 7 are also visible in Fig 4.7b which shows the spectrum produced by gating on the 1319 keV line.

Band 4, 10, 11 and 12 are new bands added to the level scheme. The spins assigned to band 4 rely on the presence of the 754 and 792 keV transitions between bands 3 and 4 and the DCO ratio of the 346 keV transition linking band 4 to band 3, which is close to unity. The spin of band 10 remains tentative because of the contradiction with the small DCO ratio (0.68(8)) of the 841 keV transition, which is assigned as a stretched E2. The transitions on band 10 are stretched E2, when gating on E2 transition and even the calculate DCO ratio indicate that transitions on band 10 are stretched E2. In this case the $\Delta I=2$ is correlating with the calculated DCO ratios.

Chapter 5 Discussion

Several new bands have been observed, including Band 7, 8, 9, 10, 11 and 12 as depicted in the constructed level scheme of ^{160}Yb. These bands are characterized by different configurations.

In the upper panel of Fig 5.1, the energies of the positive parity bands are plotted relative to a rigid rotor, while the lower panel shows the negative parity bands. Each band has its own signature depending on its configuration. Note that band 1 and band 7 lie over 1 MeV above the yrast line- thus the region where tetrahedral bands are expected has been populated, at least indirectly, as these bands are fed from higher spins.

5.1 Band 5 and Band 6

The ground states band (Band 5) is seen (Fig 5.1) to increase smoothly in energy as a function of spin until a discontinuity above spin 10, where the slope changes suddenly. This has been interpreted [Rie80] as a band crossing, where the ground state band is crossed by a band in which a pair of $i_{13/2}$ neutrons has aligned their angular momentum with the rotation of the core, due to the Coriolis force.

Thus Band 6 represents the continuation of the ground state band through the crossing, No other positive parity bands show such a crossing, but a crossing band is there in Band 1, a negative parity band.

5.2 Band 1 to 4

The negative parity side bands have been extended to lower spins states; at low spin (<8) these are interpreted as likely octupole vibrational bands. The octupole bands are on the left side of the constructed level scheme of ^{160}Yb in Fig 4.2. Octupole vibrations carry from 0 to 3 units of angular momentum.

Band 1 shows a crossing near spin 8, (Fig 5.1) which has been interpreted as a change in character from octupole to two particles. The suggested configuration is $\nu\frac{3}{2}[651]\otimes\nu\frac{3}{2}[532]$ [Rie80]. Band 2 and band 1, and is interpreted as simply the odd spin partner of band 1[Rie80]. At higher spin, band 3 has also been interpreted as a two-particle band, based on the $\nu\frac{1}{2}[660]\otimes\nu\frac{3}{2}[532]$ configuration [Rie80].

Band 4 behave differently compare with other bands and not showing any crossing band (Fig 5.1). The spin of band 4 extended up to 15ħ.

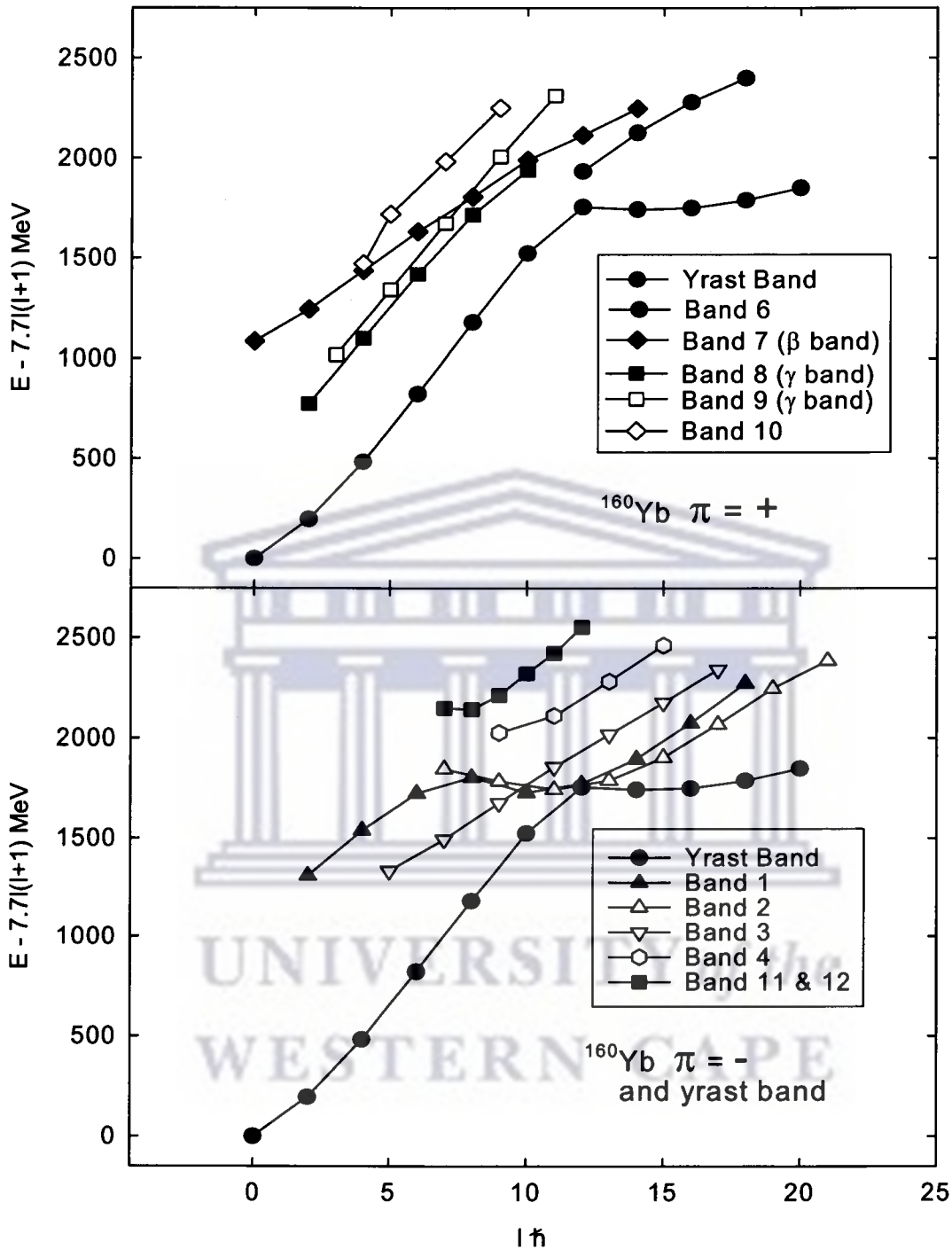

Figure 5.1: *The energies of the level after subtracting the rotational energy of a rigid rotor.*

5.3 Band 7

Band 7 is presumably the β band, but due to the loss of intensity through I→I→2 and I→I transitions to the ground band, the 0^+ bandhead could not be identified. The 0^+state shown on the level scheme is the 0^+ state, identified in β decay [Aue84]. The assignment of this level to the bandhead of band 7 is seen to be quit plausible when it is plotted as a member of the band in Fig 5.1, which shows the energies of the levels of the bands of ^{160}Yb, less a rigid rotor reference, as a function of spin, as it falls on the smooth extrapolation of the band to spin 0ħ.

5.4 Band 8 and Band 9

These two bands are interpreted as the even and odd spin sequences of the γ vibrational bands. In gamma vibration, the nucleus deforms into ellipsoidal shape in the equatorial direction (all the axis are not the same). Such a vibration carries two units of angular momentum parallel to the 3 axis. The components of angular momentum of orientation remain zero, since the moment of inertia is zero. In this case, the states of the band are 2^+, 3^+, and 4^+ etc and K = 2. G=0 because there is no other states that lie below them.

5.5 Band 10

Since only three levels of bands of band 10 have been determined, and their spin and parity is uncertain, the configuration assignment of this band is problematic. It is possibly of vibrational character, considering its decay to the γ-band.

5.6 Band 11 and 12

Band 11 and 12 occur at high excitation energy, slightly higher in energy than the 2 particle bands that cross the ground state band and the octupole band (see Fig 5.1). Therefore it is likely that they are 2-particle bands. There are only two possible configurations, namely,

$$\nu\frac{11^{-}}{2}[505]\otimes\nu\frac{3^{+}}{2}[651] \text{ or } \pi\frac{7^{-}}{2}[523]\otimes\pi\frac{7^{+}}{2}[404]$$

CHAPTER 6

Summary and Conclusion

The work presented in this thesis was based on the study of gamma coincidence data, which have been collected from the two weekends experiment performed in AFRODITE at iThemba LABS. Low spin states in ^{160}Yb produced from ^{147}Sm(^{16}O,3n)^{160}Yb have been studied. The data analysis comprises of analysis of gamma-gamma coincidence and Directional Correlation of Oriented (DCO) states measurements.

During the analysis of the data, we obtained new rotational bands and added to the constructed level scheme of ^{160}Yb. The experiment has been successful in observing states more than 1 MeV above the yrast line, where the proposed tetrahedral bands could be expected, but those bands that have been obtained in the expected energy interval, do not show the expected decay of tetrahedral bands. We interpret those new bands as beta (β) and gamma (γ) vibration bands.

The Directional Correlation of Oriented (DCO) states were measured in order to assign multipolarities of transitions from the bands in the constructed level scheme of ^{160}Yb.

References

[AFR05] AFRODITE array, Manual, iThemba LABS, (2005)

[Aue84] H. Auer, J. Fernández, H. Puchta, and F. Riess, Atoms and Nuclei 318, 323-327(1984)

[Bur79] W.E. Burcham, Elements of NUCLEAR PHYSICS, Longman group Limited 1979, page 226

[Byr87] T. Byrski, F.A. Beck, J.C. Merdinger, A. Nourreddine, H.W. Cranmer Gordon, D.V. Elenkov, P.D. Forsyth, D. Howe, M.A. Riley, J.F. Sharpey-Schafer, J. Simpson, J. Dudek and W. Nazarewicz, Nuclear Physics A474 (1987) 204

[Duc99] G. Duchene, Nuclear Instruments and Methods in Physics Research A432 (1999) 90-110

[Dud02] J. Dudek et al, Phys. Rev. Lett.88, (2002) 252505.

[Dud03] J. Dudek et al, Acta Phys. Pol. B 34 (2003) 2491

[Gar82] C. Garret, S. Rastikerdar, W.Gelletly, Phys. Rev. Lett. 118B, (1982)

[Gav93] A. Gavron, Computational Nuclear Physics 2, Nuclear Reactions, Spinger-Verlag New York, Inc, 108 (1993).

[Jen95] H.J. Jensen, PHD thesis, University of Copenhagen, (1995)

[Lil01] John Lilley, Nuclear Physics Principles and Applications, John Wiley & Sons, 2001. Page 59

[Jon95] P.M. Jones, Nuclear Instruments and Method in Physics Research A362 (1995) 556

[Kno79] G.F. Knoll, Radiation Detection and Measurements, John Willey & Sons, 1989, page 288-290

[Kra72] K.S. Krane, Nuclear Instruments and Methods 98, North-Holland and Publishing Co, (1972) 205

[Kra73] K.S. Krane, R.M. Steffen, R.M. Wheeler, Nuclear Data Tables, 11, 352(1973).

[Leo87] William R. Leo, Techniques for Nuclear and Particle Physics Experiments, Lausanne, March 1987, page 272

[Mar69] Pierre Marmier and Eric Sheldon, Physics of Nuclei and Particles, Volume 1, ACADEMIC PRESS, 1969, page 416.

[New98] R.T. Newman, Proceedings of Balkan School on Nuclear Physics, September 1-10, 1998 Baltalimani, Istanbul-TURKEY, Balkan Physics Letter 182 (1998).

[Pal83] M.K. Pal, Theory of Nuclear Structure, copyright 1983 by Affliated East-West Press Private Limited, page 524-525

[Rad95] D.C Radford. Nucl.Instr.and Meth. A361, 297(1995)

[Rie80] L.L. Riedinger et al, Physical Review Letters, Volume 44, no 9, 569 (1980)

[Won90] Samuel S.M. Wong, INTRODUCTORY NUCLEAR PHYSICS, copyright 1990 by Prentice-Hall, inc. page 261-329

[Zay87] P. Zay, Phys. A-Atomic Nulcei 328,399-407 (1987)